The clustering of galaxies in the SDSS-III Baryon Oscillation Spectroscopic Survey: measurements of the growth of structure and expansion rate at $z = 0.57$ from anisotropic clustering

Beth A. Reid,[1][*][†] Lado Samushia,[2,3] Martin White,[1,4] Will J. Percival,[2] Marc Manera,[2] Nikhil Padmanabhan,[5] Ashley J. Ross,[2] Ariel G. Sánchez,[6] Stephen Bailey,[1] Dmitry Bizyaev,[7] Adam S. Bolton,[8] Howard Brewington,[7] J. Brinkmann,[7] Joel R. Brownstein,[8] Antonio J. Cuesta,[5] Daniel J. Eisenstein,[9] James E. Gunn,[10] Klaus Honscheid,[11] Elena Malanushenko,[7] Viktor Malanushenko,[7] Claudia Maraston,[2] Cameron K. McBride,[9] Demitri Muna,[12] Robert C. Nichol,[2] Daniel Oravetz,[7] Kaike Pan,[7] Roland de Putter,[13,14] N. A. Roe,[1] Nicholas P. Ross,[1] David J. Schlegel,[1] Donald P. Schneider,[15] Hee-Jong Seo,[16] Alaina Shelden,[7] Erin S. Sheldon,[17] Audrey Simmons,[7] Ramin A. Skibba,[18] Stephanie Snedden,[7] Molly E. C. Swanson,[9] Daniel Thomas,[2] Jeremy Tinker,[12] Rita Tojeiro,[2] Licia Verde,[14,19] David A. Wake,[20] Benjamin A. Weaver,[12] David H. Weinberg,[21] Idit Zehavi[22] and Gong-Bo Zhao[2,23]

[1]*Lawrence Berkeley National Laboratory, 1 Cyclotron Road, Berkeley, CA 94720, USA*
[2]*Institute of Cosmology and Gravitation, University of Portsmouth, Dennis Sciama Building, Portsmouth P01 3FX*
[3]*National Abastumani Astrophysical Observatory, Ilia State University, 2A Kazbegi Ave., GE-1060 Tbilisi, Georgia*
[4]*Departments of Physics and Astronomy, University of California, Berkeley, CA 94720, USA*
[5]*Department of Physics, Yale University, 260 Whitney Ave, New Haven, CT 06520, USA*
[6]*Max-Planck-Institut für extraterrestrische Physik, Postfach 1312, Giessenbachstr., 85741 Garching, Germany*
[7]*Apache Point Observatory, PO Box 59, Sunspot, NM 88349-0059, USA*
[8]*Department of Physics and Astronomy, University of Utah, 115 S 1400 E, Salt Lake City, UT 84112, USA*
[9]*Harvard–Smithsonian Center for Astrophysics, 60 Garden Street, Cambridge, MA 02138, USA*
[10]*Department of Astrophysical Sciences, Princeton University, Princeton, NJ 08544, USA*
[11]*Department of Physics and CCAPP, Ohio State University, Columbus, OH 43210, USA*
[12]*Center for Cosmology and Particle Physics, New York University, New York, NY 10003, USA*
[13]*Instituto de Fisica Corpuscular, Universidad de Valencia-CSIC, Valencia 46701, Spain*
[14]*ICC, University of Barcelona (IEEC-UB), Marti i Franques 1, Barcelona 08028, Spain*
[15]*Department of Astronomy and Astrophysics and Institute for Gravitation and the Cosmos, The Pennsylvania State University, University Park, PA 16802, USA*
[16]*Berkeley Center for Cosmological Physics, LBL and Department of Physics, University of California, Berkeley, CA 94720, USA*
[17]*Brookhaven National Laboratory, Bldg 510, Upton, NY 11973, USA*
[18]*Steward Observatory, University of Arizona, 933 N. Cherry Ave., Tucson, AZ 85721, USA*
[19]*ICREA, Passeig Lluís Companys 23, Barcelona 08010, Spain*
[20]*Yale Center for Astronomy and Astrophysics, Yale University, New Haven, CT 06520, USA*
[21]*Department of Astronomy and CCAPP, Ohio State University, Columbus, OH 43210, USA*
[22]*Department of Astronomy, Case Western Reserve University, OH 44106, USA*
[23]*National Astronomy Observatories, Chinese Academy of Science, Beijing 100012, China*

ABSTRACT

We analyse the anisotropic clustering of massive galaxies from the Sloan Digital Sky Survey III Baryon Oscillation Spectroscopic Survey (BOSS) Data Release 9 (DR9) sample, which

[*]E-mail: beth.ann.reid@gmail.com
[†]Hubble Fellow.

consists of 264 283 galaxies in the redshift range $0.43 < z < 0.7$ spanning 3275 deg^2. Both peculiar velocities and errors in the assumed redshift–distance relation ('Alcock–Paczynski effect') generate correlations between clustering amplitude and orientation with respect to the line of sight. Together with the sharp baryon acoustic oscillation (BAO) standard ruler, our measurements of the broad-band shape of the monopole and quadrupole correlation functions simultaneously constrain the comoving angular diameter distance (2190 ± 61 Mpc) to $z = 0.57$, the Hubble expansion rate at $z = 0.57$ (92.4 ± 4.5 km s^{-1} Mpc^{-1}) and the growth rate of structure at that same redshift ($d\sigma_8/d\ln a = 0.43 \pm 0.069$). Our analysis provides the best current direct determination of both D_A and H in galaxy clustering data using this technique. If we further assume a Λ cold dark matter expansion history, our growth constraint tightens to $d\sigma_8/d\ln a = 0.415 \pm 0.034$. In combination with the cosmic microwave background, our measurements of D_A, H and $d\sigma_8/d\ln a$ all separately require dark energy at $z > 0.57$, and when combined imply $\Omega_\Lambda = 0.74 \pm 0.016$, independent of the Universe's evolution at $z < 0.57$. All of these constraints assume scale-independent linear growth, and assume general relativity to compute both $\mathcal{O}(10$ per cent$)$ non-linear model corrections and our errors. In our companion paper, Samushia et al., we explore further cosmological implications of these observations.

Key words: galaxies: haloes – galaxies: statistics – cosmological parameters – large-scale structure of Universe.

1 INTRODUCTION

Measurements of the cosmic distance–redshift relation using supernovae (Riess et al. 1998; Perlmutter et al. 1999; Kessler et al. 2009; Amanullah et al. 2010), the cosmic microwave background (CMB; Ade et al. 2011; Larson et al. 2011), the local expansion rate (Riess et al. 2011) and baryon acoustic oscillations (BAO; Cole et al. 2005; Eisenstein et al. 2005; Hütsi 2006; Blake et al. 2007; Padmanabhan et al. 2007; Percival et al. 2007, 2010; Okumura et al. 2008; Gaztanaga, Cabre & Hui 2009; Kazin et al. 2010; Reid et al. 2010b; Beutler et al. 2011; Blake et al. 2011a) have revealed that the expansion of the Universe is accelerating; either the energy density of the Universe is dominated by an exotic 'dark energy', or general relativity (GR) requires modification. The observed anisotropic clustering of galaxies can help distinguish between these possibilities by allowing simultaneous measurements of both the geometry of the Universe and the growth rate of structure.

Galaxy redshift surveys provide a powerful measurement of the growth rate through redshift–space distortions (RSD) (Kaiser 1987). Although we expect the clustering of galaxies in real space to have no preferred direction, galaxy maps produced by estimating distances from redshifts obtained in spectroscopic surveys reveal an anisotropic galaxy distribution (Cole, Fisher & Weinberg 1995; Peacock et al. 2001; Percival et al. 2004; da Angela et al. 2008; Guzzo et al. 2008; Okumura et al. 2008; Blake et al. 2011b; Samushia, Percival & Raccanelli 2012a). This anisotropy arises because the recession velocities of galaxies, from which distances are inferred, include components from both the Hubble flow and peculiar velocities driven by the clustering of matter (see Hamilton 1998, for a review). Despite the fact that galaxy light does not faithfully trace the mass, even on large scales, galaxies are expected to act nearly as test particles within the cosmological matter flow. Thus, the motions of galaxies carry an imprint of the rate of growth of large-scale structure and allow us to both probe dark energy and test GR (see e.g. Jain & Zhang 2008; Neseris & Perivolaropoulos 2008; Percival & White 2008; Song & Koyama 2009; Song & Percival 2009; McDonald & Seljak 2009; White, Song & Percival 2009; Song et al. 2010, 2011; Zhao et al. 2010, for recent studies).

The observed BAO feature in the power spectrum and correlation function of galaxies has been used to provide strong constraints on the geometry of the Universe. While the BAO method is expected to be highly robust to systematic uncertainties (see e.g. Eisenstein & White 2004; Padmanabhan & White 2009; Seo et al. 2010; Mehta et al. 2011), it does not exploit the full information about the cosmological model available in the two-dimensional clustering of galaxies. Additional geometric information is available by comparing the amplitude of clustering along and perpendicular to the line of sight (LOS); this is known as the Alcock–Paczynski (AP) test (Alcock & Paczynski 1979; Matsubara & Suto 1996; Ballinger, Peacock & Heavens 1996). RSD and AP tests rely on the measurements of anisotropy in the statistical properties of the galaxy distribution and are partially degenerate with each other, so that constraints on the growth of structure from RSD depend on the assumptions about the background geometry and vice versa (Samushia et al. 2012a). However, given high precision clustering measurements over a wide range of scales, this degeneracy can be broken since RSD and AP have different scale-dependences. Recently, the WiggleZ survey (Drinkwater et al. 2010) has performed a joint RSD and AP analysis that constrains the expansion history in four bins across $0.1 < z < 0.9$ at the 10–15 per cent level (Blake et al. 2011c). Using the Sloan Digital Sky Survey II (SDSS-II) luminous red galaxy (LRG) sample, Chuang & Wang (2012) perform a similar analysis to the present work. They measure the angular diameter distance $D_A(z = 0.35) = 1048^{+60}_{-58}$ Mpc and the Hubble expansion rate $H(z = 0.35) = 82.1^{+4.8}_{-4.9}$ km s^{-1} Mpc^{-1} at $z = 0.35$ after marginalizing over RSDs and other parameter uncertainties.

Obtaining reliable cosmological constraints from the RSD and AP effects demands precise modelling of the non-linear evolution of both the matter density and velocity fields, as well as the ways in which the observed galaxies trace those fields. The halo model of large-scale structure and variants thereof assumes that galaxies form and evolve in the potential wells of dark matter haloes, and provides a successful means of parametrizing the relation between the galaxy and halo density and velocity fields. Our modelling approach, based on Reid & White (2011), uses perturbation theory to account for the non-linear redshift space clustering of haloes in

the quasi-linear regime as a function of cosmological parameters, and then uses the halo model framework to motivate our choice of nuisance parameters describing the galaxy–halo relation. We test these assumptions with a large volume of mock galaxy catalogues derived from *N*-body simulations.

The ongoing Baryon Oscillation Spectroscopic Survey (BOSS; Schlegel, White & Eisenstein 2009), which is part of SDSS-III (Eisenstein et al. 2011), is measuring spectroscopic redshifts of 1.5 million galaxies, approximately volume limited to $z \simeq 0.6$ (in addition to spectra of 150 000 quasars and various ancillary observations). The galaxies are selected from the multi-colour SDSS imaging to probe large-scale structure at intermediate redshift; they trace a large cosmological volume while having high enough number density to ensure that shot-noise is not a dominant contributor to the clustering variance (White et al. 2011). The resulting clustering measurements provide strong constraints on the parameters of standard cosmological models.

We use the CMASS sample of BOSS galaxies that will be included in SDSS Data Release 9 (DR9) to constrain the growth of structure and geometry of the Universe. We apply RSD and AP tests to the data to measure the growth rate, the Hubble expansion rate and the comoving angular diameter distance at $z_{\mathrm{eff}} = 0.57$. We improve on previous, similar analyses in a number of ways. First, we use a model for the non-linear anisotropic correlation function that is accurate to well below our statistical errors over the wide range of scales between $25\,h^{-1}$ Mpc and $160\,h^{-1}$ Mpc, which we validate using $68\,(h^{-1}\,\mathrm{Gpc})^3$ of *N*-body simulations populated with mock CMASS galaxies. Next, rather than assuming a fixed underlying linear matter power spectrum, we use a prior on $P(k)$ based on the 7 year *Wilkinson Microwave Anisotropy Probe* (WMAP7) CMB constraints (Komatsu et al. 2011; Larson et al. 2011) and marginalize over the remaining uncertainties for all fits. In addition to joint constraints on the geometric (BAO and AP) and peculiar velocity (RSD) parameters, we present three 'null' tests of the Λcold dark matter (ΛCDM) model. To begin, we simply ask whether any points in the ΛCDM parameter space allowed by *WMAP7* provide a good fit to the CMASS clustering; in this case, the only free parameters are those describing how galaxies trace matter. In the other two tests, we fit for the amplitude of peculiar velocities using *WMAP7* priors on geometric quantities, or we fit for the geometric parameters with *WMAP7* priors on RSD. Thus we can present the statistical precision with which our data measure either peculiar velocities or the AP effect in the ΛCDM model. Finally, given the strong detection of the BAO feature in the monopole of the correlation function, we can break the degeneracy between $(1 + z_{\mathrm{eff}})D_{\mathrm{A}}$ and H with our AP measurement. We present the most constraining measurement of $H(z_{\mathrm{eff}})$ from galaxy clustering data to date using this technique, even after marginalizing over the amplitude of the RSD effect. As our constraints exploit the full shape of the monopole and quadrupole correlation functions, they rely on further assumptions about the cosmological model: Gaussian, adiabatic, power-law primordial perturbations, the standard number $N_{\mathrm{eff}} = 3.04$ of massless neutrino species (see discussion in Komatsu et al. 2011), and that dark matter is 'cold' on the relatively large scales of interest. Our analysis relies on the validity of GR in several ways, and so interpretation of our constraints in modified gravity scenarios must proceed with caution. In particular, we assume that the linear growth of matter perturbations is scale-independent, compute non-linear corrections in perturbation theory assuming GR, calibrate our treatment of small-scale galaxy velocities using GR *N*-body simulations, and estimate the covariance matrix for our measurements using the Lagrangian perturbation theory (LPT), which assumes GR.

This paper is organized as follows. In Section 2 we describe BOSS DR9 CMASS data and in Section 3 we describe the measurements of the two-dimensional clustering of galaxies used in this analysis. Section 4 reviews the theory of the RSD and AP effects, and describes the theoretical model used to fit the observed galaxy correlation function. Section 5 outlines the cosmological model space in which we derive the constraints presented in Section 6 on the shape of the linear matter power spectrum, growth rate of cosmic structure, angular diameter distance to and expansion rate at $z = 0.57$. We conclude by discussing the cosmological implications of our results in Section 7.

2 DATA

BOSS targets for spectroscopy luminous galaxies selected from the multi-colour SDSS imaging (Fukugita et al. 1996; Gunn et al. 1998, 2006; York et al. 2000). The target selection algorithms are summarized by Eisenstein et al. (2011) and Anderson et al. (2012). For the galaxy sample referred to as 'CMASS', colour–magnitude cuts are applied to select a roughly volume-limited sample of massive, luminous galaxies; see Masters et al. (2011) for a detailed examination of the properties of CMASS targets in the COSMOS field. The majority of the galaxies are old stellar systems whose prominent 4000 Å break in their spectral energy distributions makes them relatively easy to select in multi-colour data. Most CMASS galaxies are central galaxies residing in dark matter haloes of $10^{13}\,h^{-1}\,\mathrm{M}_{\odot}$, but a non-negligible fraction are satellites which live primarily in haloes about 10 times more massive (White et al. 2011). These galaxies are intrinsically very luminous and at the high mass end of the stellar mass function (Maraston et al. 2012). Galaxies in the CMASS sample are highly biased ($b \sim 2$; White et al. 2011). In addition, they trace a large cosmological volume while having high enough number density to ensure that shot-noise is not a dominant contributor to the clustering variance, which makes them particularly powerful for probing statistical properties of large-scale structure.

Anderson et al. (2012) detail the steps for generating the large-scale structure catalogue and mask for DR9 (Ahn et al. 2012; Bolton et al. 2012; Dawson et al. 2012; Smee et al. 2012), which includes the data taken by BOSS through 2011 July and covers 3275 deg² of sky. In our analysis we use galaxies from the BOSS CMASS DR9 catalogue in the redshift range of $0.43 < z < 0.70$. The sample includes a total of 264 283 galaxies, 207 246 in the north and 57 037 in the south Galactic hemispheres. Fig. 1 shows the redshift distribution and Fig. 2 shows the angular distribution of the galaxies in our sample.

3 MEASUREMENTS

3.1 Two-point statistics

To compute redshift space separations for each pair of galaxies given their angular coordinates and redshifts, we must adopt a cosmological model. We use the same one as used to generate our mock catalogues, namely spatially flat ΛCDM with $\Omega_{\mathrm{m}} = 0.274$. This is the same cosmology as assumed in White et al. (2011) and in our companion papers (Anderson et al. 2012; Manera et al. 2012; Ross et al. 2012; Sanchez et al. 2012; Samushia et al. 2012b; Tojeiro et al. 2012). Our model accounts for this assumption and scales the theory prediction accordingly when testing a cosmological model with a different distance–redshift relation (see Section 4.5).
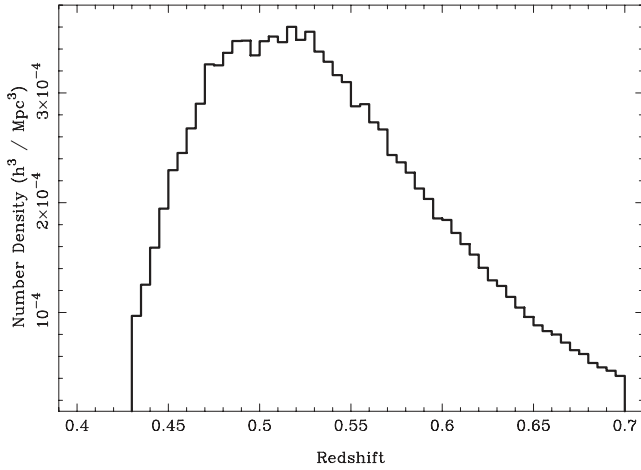
Figure 1. Number density as a function of redshift for the CMASS galaxies used in this analysis. After accounting for our weighting scheme, the effective redshift for galaxy pairs in this sample is $z_{eff} = 0.57$.
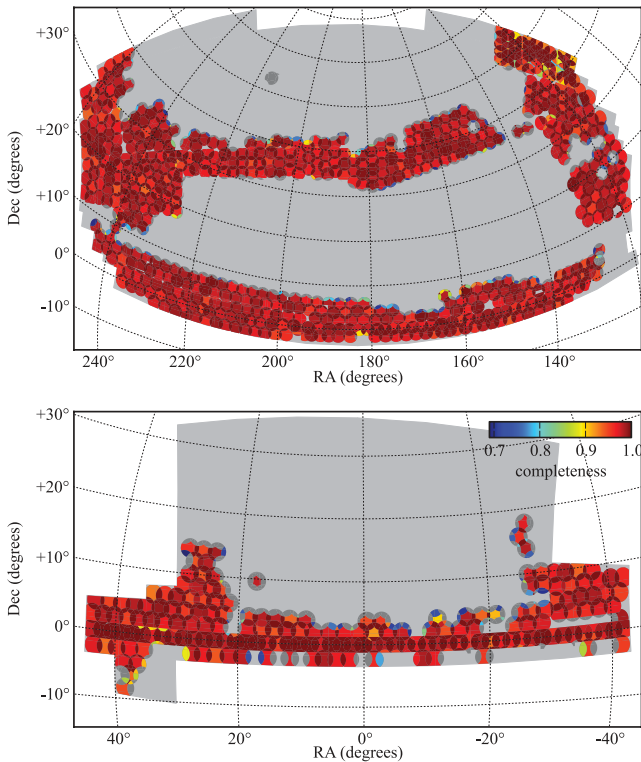
Figure 2. BOSS DR9 sky coverage. The light grey region shows the expected total footprint of the survey, while the colours indicate completeness in the DR9 spectroscopy for regions included in our analysis. Dark grey regions are removed from the analysis by completeness or redshift failure cuts [see section 3.5 of Anderson et al. (2012) for further details].

Using the galaxy catalogue of Anderson et al. (2012) we compute weighted 'data-data' (DD) pair counts in bins of s and μ

$$DD(s_i, \mu_j) = \sum_{k=1}^{N_{tot}} \sum_{l=k+1}^{N_{tot}} \Theta_{k,l}(s_i, \mu_j) w_k(s_i) w_l(s_i), \quad (1)$$

where s is the comoving pair separation in redshift space, μ is the cosine of the angle between the pair separation vector and the LOS, and w_k is the weight of kth galaxy in the catalogue. The double sum runs over all galaxies and $\Theta_{k,l}(s_i, \mu_j) = 1$ if the pair separation

between two galaxies falls into bin s_i, μ_j, and is zero otherwise. We bin s in 23 equal logarithmic bins between $s_{min} = 25.1$ and $s_{max} = 160 \, h^{-1}$ Mpc with $d\log_{10}s = 0.035$, and 200 equally spaced μ bins between 0 and 1.

Three distinct effects contribute to the final weight w_i of each galaxy. These weights are described in more detail in Anderson et al. (2012) and Ross et al. (2012). First, galaxies lacking a redshift due to fibre collisions or because their spectrum was not adequate to secure a redshift are accounted for by upweighting the nearest galaxy by weight $w = (1 + n)$, where n is the number of near neighbours without a redshift. Secondly, we use the minimum variance weighting of Davis & Huchra (1982) and Hamilton (1993),

$$w(s) = \frac{1}{1 + J_3(s)\bar{n}(z)}, \quad (2)$$

where $\bar{n}(z)$ is the expected number density of galaxies at the redshift of the galaxy and

$$J_3(s) = 2\pi \int_0^s s'^2 \, ds' \, d\mu \, \xi(s', \mu) \quad (3)$$

is the angularly averaged redshift–space correlation function integrated up to the separation of galaxies in the pair. For every galaxy this weight will vary depending on which pair-counting bin it is assigned. For a constant radial selection function this weighting scheme results in the minimal variance of the estimated correlation function (for details see Hamilton 1993). Note that the analyses in Sanchez et al. (2012) and Anderson et al. (2012) use scale-independent weights; differences between the approaches are small in practice.

The third weight corrects for angular systematics, related to the angular variations in density of stars that make detection of galaxies harder in areas of sky closer to the Galactic equator (for details see Ross et al. 2012). The total weight is the product of these three weights. We compute 'data–random' (DR) and 'random–random' (RR) pair counts as in equation (1), except that each random point is assigned only the $J_3(s)$ weight and not the close-pair correction and systematic weights. Positions of objects in our random catalogue are generated using the observational mask and redshifts are generated by picking a random redshift drawn from the measured redshifts of observed galaxies. Our random catalogues contain approximately 70 times more objects than the galaxy catalogue.

Following Landy & Szalay (1993), the pair counts are combined to estimate the anisotropic correlation function as:

$$\hat{\xi}_{LS}(s_i, \mu_j) = \frac{DD(s_i, \mu_j) - 2DR(s_i, \mu_j) + RR(s_i, \mu_j)}{RR(s_i, \mu_j)}. \quad (4)$$

Fig. 3 shows our measurement of $\hat{\xi}_{LS}(s_i, \mu_j)$ in terms of LOS separation $r_\pi = s\mu_s$ and transverse separation $r_\sigma = s(1 - \mu^2)^{1/2}$. The central 'squashing' is due to peculiar velocities. In the left-hand panel, the BAO ridge at ~100 h^{-1} Mpc is evident. In the right-hand panel, we show the clustering signal on smaller scales; the 'finger-of-God' effect is visible for small transverse separations but small on the scales we analyse. The innermost contour in the right-hand panel indicates the value of ξ_0 in the smallest separation bin included in our cosmological analysis.

Rather than work with the two-dimensional correlation function $\xi(s, \mu_s)$, we conduct our cosmological analysis on the first two even Legendre polynomial moments, $\xi_0(s)$ and $\xi_2(s)$, defined by

$$\xi_\ell(s) = \frac{2\ell + 1}{2} \int d\mu_s \, \xi(s, \mu_s) L_\ell(\mu_s), \quad (5)$$
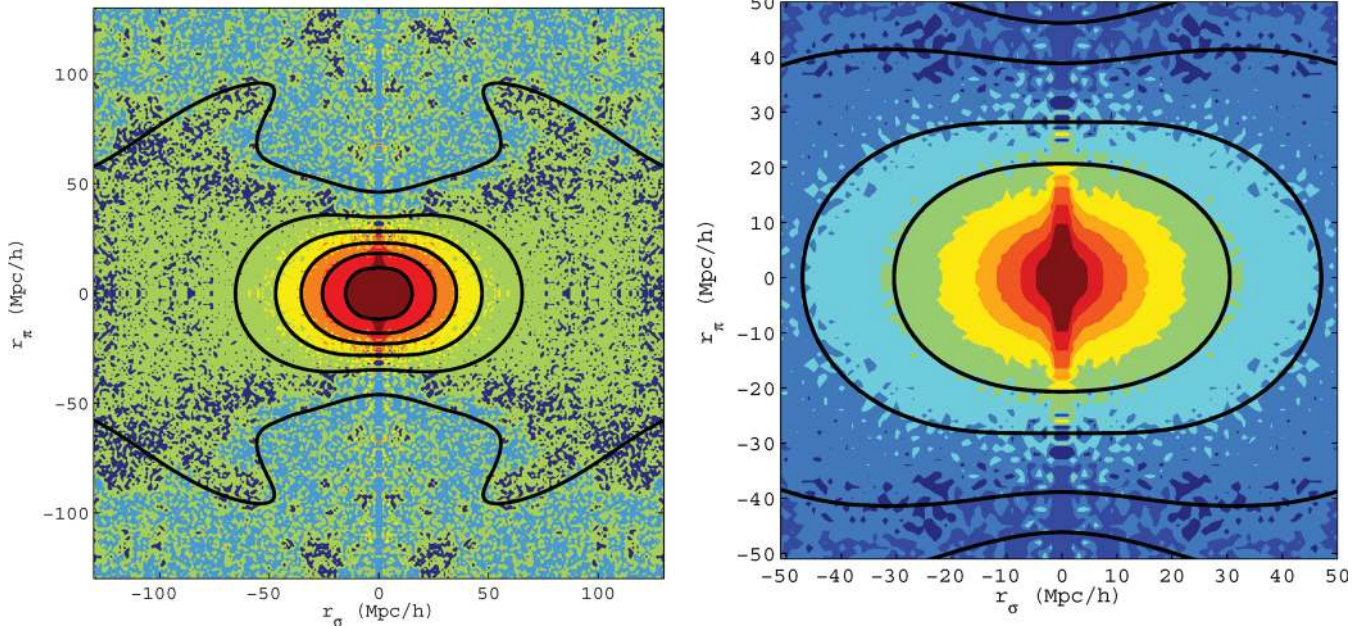
Figure 3. Left-hand panel: two-dimensional correlation function of CMASS galaxies (colour) compared with the best-fitting model described in Section 6.1 (black lines). Contours of equal ξ are shown at [0.6, 0.2, 0.1, 0.05, 0.02, 0]. Right-hand panel: smaller-scale two-dimensional clustering. We show model contours at [0.14, 0.05, 0.01, 0]. The value of ξ_0 at the minimum separation bin in our analysis is shown as the innermost contour. The $\mu \approx 1$ 'finger-of-God' effects are small on the scales we use in this analysis.

or equivalently (Hamilton 1992),

$$\xi(s, \mu_s) \equiv \sum_{\ell=0}^{\infty} \xi_\ell(s) L_\ell(\mu_s). \tag{6}$$

Here L_ℓ is the Legendre polynomial of order ℓ. By symmetry all odd-ℓ moments vanish and on large scales the measurements become increasingly noisy to larger ℓ. The correlation functions $\hat{\xi}_0(s)$ and $\hat{\xi}_2(s)$ are estimated from $\hat{\xi}_{\rm LS}(s_i, \mu_j)$ using a Riemann sum to approximate equation (5). We include all galaxy pairs between 25 and $160\,h^{-1}$ Mpc in our analysis. We also caution the reader that we have adopted logarithmically spaced bins, while our companion papers (Anderson et al. 2012; Ross et al. 2012; Sanchez et al. 2012) analyse clustering in linearly spaced bins of differing bin sizes. Our measurements of ξ_0 and ξ_2, along with diagonal errors estimated from PTHalos mock catalogues (Manera et al. 2012; see Section 3.2), are shown in Fig. 4. The effective redshift of weighted pairs of galaxies in our sample is $z = 0.57$, with negligible scale dependence for the range of interest in this paper. For the purposes of constraining cosmological models, we will interpret our measurements as being at $z = 0.57$.

3.2 Covariance matrices

The matrix describing the expected covariance of our measurements of $\xi_\ell(s)$ in bins of redshift space separation depends in linear theory only on the underlying linear matter power spectrum, the bias of the galaxies, the shot-noise (often assumed Poisson) and the geometry of the survey. We use 600 PTHalos mock galaxy catalogues to estimate the covariance matrix of our measurements. These mocks are based on combining LPT with the halo model, and are described in more detail in Manera et al. (2012). We compute $\xi_\ell(s_i)$ for each mock in exactly the same way as from the data (Section 3.1) and
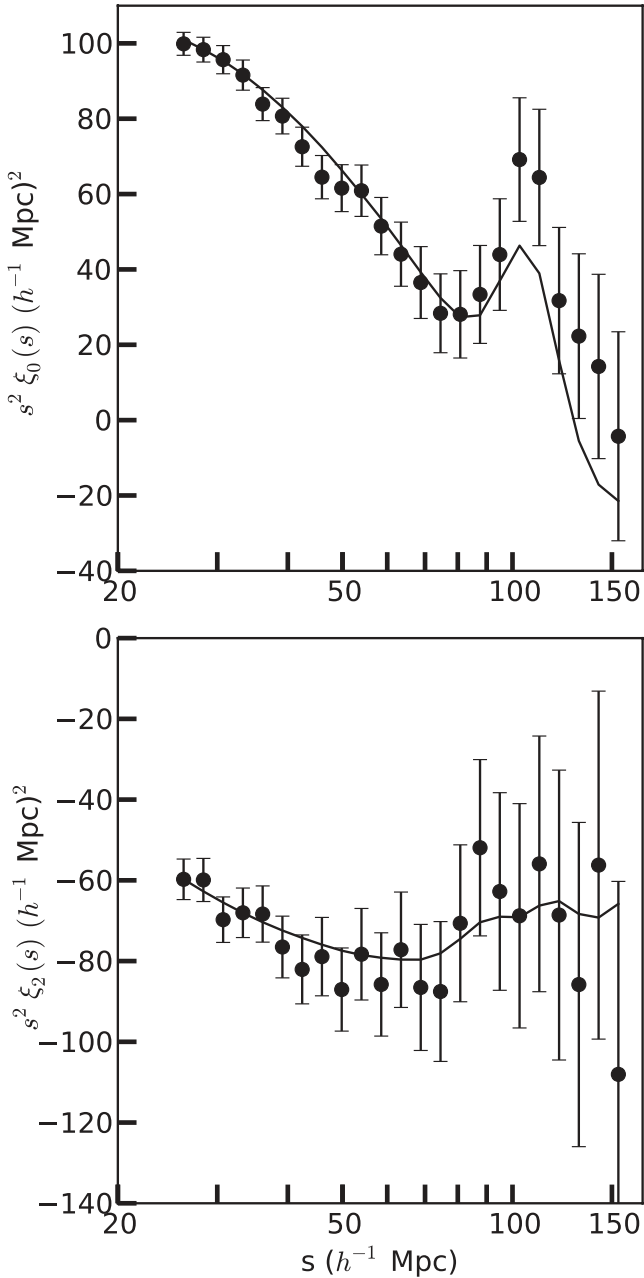
estimate the covariance matrix as

$$C_{ij}^{\ell_1 \ell_2} = \frac{1}{599} \sum_{k=1}^{600} \left(\xi_{\ell_1}^k(s_i) - \bar{\xi}_{\ell_1}(s_i) \right) \left(\xi_{\ell_2}^k(s_j) - \bar{\xi}_{\ell_2}(s_j) \right), \tag{7}$$

where $\xi_\ell^k(s_i)$ is the monopole ($\ell = 0$) or quadrupole ($\ell = 2$) correlation function for pairs in the ith separation bin in the kth mock. $\bar{\xi}_\ell(s)$ is the mean value over all 600 mocks. The shape and amplitude of the average two-dimensional correlation function computed from the mocks are a good match to the measured correlation function of the CMASS galaxies [see Manera et al. (2012) and Ross et al. (2012) for more detailed comparisons]. The square roots of the diagonal elements of our covariance matrix are shown as the error bars accompanying our measurements in Fig. 4. We will examine the off-diagonal terms in the covariance matrix via the correlation matrix, or 'reduced covariance matrix', defined as

$$C_{ij}^{\ell_1 \ell_2, \rm red} = C_{ij}^{\ell_1 \ell_2} / \sqrt{C_{ii}^{\ell_1 \ell_1} C_{jj}^{\ell_2 \ell_2}}, \tag{8}$$

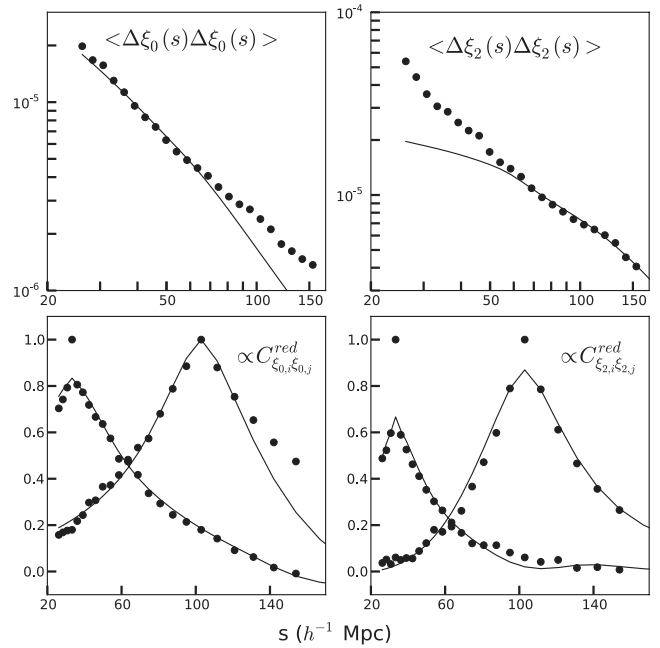where the division sign denotes a term-by-term division.

In Fig. 5 we compare selected slices of our mock covariance matrix (points) to a simplified prediction from linear theory (solid lines) that assumes a constant number density $\bar{n} = 3 \times 10^{-4}\,(h^{-1}\,{\rm Mpc})^{-3}$ and neglects the effects of survey geometry (see e.g. Tegmark 1997). Xu et al. (2012) performed a detailed comparison of linear theory predictions with measurements from the Las Damas SDSS-II LRG mock catalogues (McBride et al., in preparation), and showed that a modified version of the linear theory covariance with a few extra parameters provides a good description of the N-body based covariances for $\xi_0(s)$. The same seems to be true here as well. The mock catalogues show a deviation from the naive linear theory prediction for $\xi_2(s)$ on small scales; a direct consequence is that our errors on quantities dependent on the quadrupole are larger than a simple Fisher analysis would indicate. We verify that the same qualitative behaviour is seen for the diagonal elements of the quadrupole covariance matrix in our smaller set of N-body simulations used

Figure 4. $\xi_0(s)$ and $\xi_2(s)$ measured from BOSS CMASS galaxies. The error bars correspond to diagonal elements of the covariance matrix. The best-fitting model described in Section 6.1 is shown as the solid curve. We use 23 logarithmically spaced bins and include pairs between 25 and 160 h^{-1} Mpc.

Figure 5. Upper panels: diagonal elements of the monopole and quadrupole components of the covariance matrix computed from the PTHalos mocks (points) compared with the linear theory prediction (solid lines). Lower panels: two slices through the reduced covariance matrices $C_{ij}^{00,\mathrm{red}}$ and $C_{ij}^{22,\mathrm{red}}$ for separation bins of 33 and 103 h^{-1} Mpc. Linear theory predictions for the reduced covariance matrices in the lower panels have been scaled by a constant factor to produce good agreement between linear theory and mock covariances for off-diagonal elements, demonstrating that the scale dependence of the off-diagonal terms matches the mock covariance matrix well, but that there is extra diagonal covariance in the mocks compared with linear theory. Elements of C^{02} are small (not shown).

additional diagonal term. Finally, while not shown here, the reduced covariances between ξ_0 and ξ_2 are small.

Our analysis uses the PTHalos mock-based covariance matrix, which accurately accounts for both complexities of the survey geometry and non-linear corrections to the growth of structure on the relatively large scales of interest here, and this allows us to accurately report uncertainties associated with both our measurements and parameter fits.

4 THEORY

4.1 Redshift–space distortions: Linear theory

The effects of RSDs in the linear regime are well-known (Kaiser 1987; Fisher 1995, see also Hamilton 1998 for a comprehensive review). We briefly summarize them here. The redshift-space position, s, of a galaxy differs from its real-space position, x, due to its peculiar velocity,

$$s = x + v_z(x)\widehat{z}, \tag{9}$$

where $v_z(x) \equiv u_z(x)/(aH)$ is the change in the apparent LOS position of a galaxy due to the contribution of the LOS peculiar velocity u_z to the galaxy's redshift. Since overdensities on large, linear scales grow in a converging velocity field ($\nabla \cdot v = -f\delta_m$), the effect of peculiar velocities induces a coherent distortion in the measured clustering of galaxies that allows us to measure the amplitude of the peculiar velocity field. In linear theory, and with some approximations, the anisotropic galaxy power spectrum becomes (Kaiser

to calibrate the model correlation function. This comparison suggests that the PTHalos mocks are not underestimating the errors on ξ_2, though more *N*-body simulations (and an accounting of survey geometry) would be required for a detailed check of the PThalos mocks.

The lower panels of Fig. 5 compare the reduced covariance matrix to linear theory, where we have scaled the C_{ij}^{red} prediction from linear theory down by a constant, c_i. This comparison demonstrates that the scale dependences of the off-diagonal terms in the covariance matrix are described well by linear theory, but that the non-linear evolution captured by the PTHalos mocks can be parametrized simply as an

1987)

$$P_g^s(k, \mu_k) = \left(b + f\mu_k^2\right)^2 P_m^r(k) = b^2 \left(1 + \beta\mu_k^2\right)^2 P_m^r(k), \quad (10)$$

where b is the linear galaxy bias, $\delta_g = b\delta_m$, $f \equiv \mathrm{d}\ln\sigma_8/\mathrm{d}\ln a$ is the logarithmic growth rate of matter fluctuations, and μ_k is the cosine of the angle between $\boldsymbol{k}$ and the LOS.

4.2 Legendre moments of $\xi(r)$

In linear theory (equation 10), only the $\ell = 0$, 2 and 4 moments contribute to the power spectrum $P_g^s(\boldsymbol{k})$, and its Fourier transform $\xi_g^s(\boldsymbol{s})$. The two are simply related by ℓth order spherical Bessel functions of the first kind:

$$\xi_\ell(s) = i^\ell \int \frac{k^2 \mathrm{d}k}{2\pi^2} P_\ell(k) j_\ell(ks). \quad (11)$$

Given a tight constraint on the underlying *shape* of the linear matter power spectrum, the two-dimensional clustering of galaxies constrains both $b\sigma_8$ and $f\sigma_8$ (Percival & White 2008; White et al. 2009). In this work we measure and model only the monopole and quadrupole moments of the correlation function, $\xi_{0,2}(s)$. These two moments are sufficient to constrain both $b\sigma_8$ and $f\sigma_8$ and encompass most of the available information on the peculiar velocity field for the highly biased galaxies of interest here (see fig. 5 of Reid & White 2011). The AP effect can transfer cosmological information into higher order multipoles (Taruya, Saito & Nishimichi 2011; Kazin, Sanchez & Blanton 2012), but we do not attempt to recover this information for several reasons. First, our best-fitting AP parameter is very close to the fiducial value we have assumed, so that the mixing of multipoles is expected to be minimal. Secondly, non-linear corrections are of the order of unity for ξ_4, even for the clustering of dark matter haloes on the relatively large scales we analyse in this paper (see fig. 6 of Reid & White 2011). Moreover, we expect $\ell \geq 4$ multipoles to be more severely affected by the detailed properties of the small-scale galaxy velocities, since they weight $\mu \approx 1$ more heavily; thus, our model is less accurate for larger ℓ. Finally, fig. 6 of Ross et al. (2012) shows that we do not expect to detect ξ_4 with high significance, given the current uncertainty predicted from the PTHalos mock catalogues. Therefore, we collapse the anisotropic clustering information in $\xi(r_\sigma, r_\pi)$ into two one-dimensional functions $\xi_{0,2}(s)$ before extracting cosmological information from the anisotropic galaxy clustering.

4.3 Redshift space halo clustering in the quasi-linear regime

The Kaiser formula describing the linear effect of RSDs breaks down even on quite large scales. An accurate model of the two-dimensional clustering of galaxies must account for non-linear evolution in the real space matter density and velocity fields, non-linear galaxy bias, and the non-linear mapping between real and redshift space separations of pairs of galaxies. The simplest picture of galaxy formation asserts that galaxies occupy dark matter haloes, and so as a step towards understanding the clustering of galaxies, Reid & White (2011) showed that a streaming model where the pairwise velocity probability distribution function is approximated as Gaussian can be used to relate real space clustering and pairwise velocity statistics of haloes to their clustering in redshift space. We will demonstrate in Section 4.4 that the same model describes the clustering of galaxies:

$$1 + \xi_g^s(r_\sigma, r_\pi) =$$
$$\int \left[1 + \xi_g^r(r)\right] \mathrm{e}^{-[r_\pi - y - \mu v_{12}(r)]^2/2\sigma_{12}^2(r,\mu)} \frac{\mathrm{d}y}{\sqrt{2\pi\sigma_{12}^2(r,\mu)}}, \quad (12)$$

where r_σ and r_π are the redshift space transverse and LOS distances between two objects with respect to the observer, y is the *real* space LOS pair separation, $\mu = y/r$, ξ_g^r is the real space galaxy correlation function, $v_{12}(r)$ is the average infall velocity of galaxies separated by real-space distance r, and $\sigma_{12}^2(r, \mu)$ is the rms dispersion of the pairwise velocity between two galaxies separated with transverse (LOS) real space separation r_σ (y).

$\xi_g^r(r)$, $v_{12}(r)$ and $\sigma_{12}^2(r, \mu)$ are computed in the framework of Lagrangian (ξ^r) and standard perturbation theories (v_{12}, σ_{12}^2). Only two nuisance parameters are necessary to describe the clustering of a sample of haloes or galaxies in this model: $b_{1L} = b - 1$, the first-order Lagrangian host halo bias in *real* space, and σ_{FoG}^2, an additive, isotropic velocity dispersion accounting for small-scale motions of haloes and galaxies which will be described below. Further details of the model, its numerical implementation and its accuracy can be found in Reid & White (2011) and Appendix B.

4.4 From haloes to galaxies

Reid & White (2011) examined the validity of equation (12) only for halo clustering rather than galaxies, thus the model must be extended and checked with a realistic sample of mock galaxies. We use the machinery of the halo model (see Cooray & Sheth 2002, for a review) to describe the galaxy density field in terms of the density field of the host haloes. Of particular importance for modelling RSDs is the distinction between 'central' and 'satellite' galaxies (Kauffmann, White & Guiderdoni 1993; Cole et al. 1994; Diaferio & Geller 1996; Kravtsov et al. 2004). When modelling an approximately mass-limited galaxy sample, the first galaxy assigned to a host halo is considered central, and its position and velocity are that of the host halo centre. Satellite galaxies orbit in the potential well of the host haloes, and so are offset in both position and velocity from the halo centre. In our particular implementation of the halo model, satellite galaxies are randomly drawn from the dark matter particle members of the host halo in our simulation. As the virial velocities of massive haloes can be large (amounting to redshift space LOS separations of tens of h^{-1} Mpc), intrahalo velocities (IHV) can distort the redshift space correlation function. In the limit that these virial motions are uncorrelated with the quasi-linear velocity field of interest, they can be accounted for by additional convolution along the LOS.

To assess the impact of virial motions on the observed galaxy clustering we use the mock catalogues described in White et al. (2011), which closely match the small-scale clustering of CMASS galaxies. We compute $\xi_{0,2}(s)$ from these mocks (the average is shown as the error bars in Fig. 6) and recompute $\xi_{0,2}$ after artificially setting the IHV to 0 (the dashed curves, with the one for ξ_0 covered by the solid line). Intrahalo velocities suppress the amplitude of ξ_2 on the smallest scales we attempt to model, reaching a 10 per cent correction at $25\,h^{-1}$ Mpc. The reason for this suppression is that, on small scales, $\mathrm{d}\xi^r/\mathrm{d}y < 0$ and non-negligible. This causes a net transport of pairs to larger separations in redshift space. Note this is opposite to the effect of quasi-linear peculiar velocities, which make the separation of a pair in redshift space on average smaller than in real space.

We include the effect of IHV in our model by including an extra convolution with a Gaussian of dispersion σ_{FoG}. The solid curves in Fig. 6 are then the predictions for $\xi_{0,2}$ with the best fit $\sigma_{FoG}^2 = (3.2\,h^{-1}\,\mathrm{Mpc})^2$ or $21\,\mathrm{Mpc}^2$. The model successfully describes the effect of IHV on the monopole and quadrupole correlation functions.
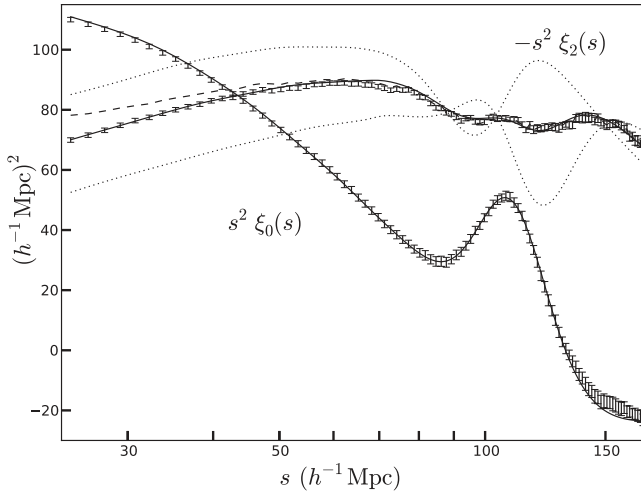
Figure 6. Error bars enclose the mean $s^2\xi_{0,2}(s)$ measured from the White et al. (2011) mock galaxy catalogues. The solid line is our model fit, where $\sigma_{\rm FoG}^2$ has been varied to minimize the difference. The dashed line shows $s^2\xi_2$ for the mock galaxies when their IHV are artificially set to 0, and indicates that IHV suppress ξ_2 by $\approx$10 per cent on the smallest scales we are fitting. The nuisance parameter $\sigma_{\rm FoG}^2$ adequately describes the effect of IHV. Dotted lines show the predicted ξ_2 when varying the AP parameter $F(z)$ by $\pm$10 per cent and holding D_V (and thus ξ_0) fixed.

In Appendix B4 we quantify the impact of our uncertainties in the halo occupation distribution (HOD) of CMASS galaxies and the possible breakdown of our assumption that the first galaxy assigned to each halo is 'central' (i.e. has no intrahalo velocity dispersion) on the value of our nuisance parameter $\sigma_{\rm FoG}^2$. As a result of these considerations, we place a uniform prior on $\sigma_{\rm FoG}^2$ between 0 and 40 (Mpc)^2.

4.5 Alcock–Paczynski effect

Galaxy redshift surveys collect two angular coordinates and a redshift for each galaxy in the sample. A fiducial cosmological model must be adopted to generate maps and measure clustering as a function of comoving separations. This mapping depends on both the angular diameter distance and the inverse of the Hubble parameter at the redshift of each galaxy pair. To a good approximation the inferred galaxy clustering in a different cosmological model can be obtained from the fiducial one by a single rescaling of the transverse and parallel separations (Percival et al. 2010). Rather than modify our observed galaxy clustering, we will account for the AP effect when we test different cosmological models by introducing two scale parameters, $\alpha_\perp$ and $\alpha_\parallel$, into the theoretical correlation functions we are fitting to:

$$\xi^{\rm fid}(r_\sigma, r_\pi) = \xi^{\rm true}(\alpha_\perp r_\sigma, \alpha_\parallel r_\pi), \tag{13}$$

$$\alpha_\perp = \frac{D_{\rm A}^{\rm fid}(z_{\rm eff})}{D_{\rm A}^{\rm true}(z_{\rm eff})}, \qquad \alpha_\parallel = \frac{H^{\rm true}(z_{\rm eff})}{H^{\rm fid}(z_{\rm eff})}, \tag{14}$$

where $D_{\rm A}$ denotes the physical angular diameter distance. Here $\xi^{\rm true}$ is the expected two-dimensional correlation function *if the* measured galaxy correlation function were computed assuming the true redshift–distance relation in the cosmology being tested. $\xi^{\rm fid}$ is the prediction for the measured correlation function, given that galaxy separations were computed using the fiducial cosmology model. That is, $\alpha_\perp$ and $\alpha_\parallel$ scale the 'true' separations to the ones calculated using the fiducial cosmology.

The spherically averaged correlation function, ξ_0, is sensitive to the parameter combination

$$D_V(z) \equiv \left((1+z)^2 D_{\rm A}^2(z) \frac{cz}{H(z)} \right)^{1/3}. \tag{15}$$

The quadrupole of the measured correlation function allows a measurement of a second combination (Alcock & Paczynski 1979; Padmanabhan & White 2008; Blake et al. 2011c)

$$F(z) = (1+z)D_{\rm A}(z)H(z)/c, \tag{16}$$

thus breaking the degeneracy between $(1 + z_{\rm eff})D_{\rm A}$ and H. To a good approximation, changing D_V simply rescales the value of s in the predicted correlation function, while F primarily affects the quadrupole. Fig. 6 shows the effect of varying F by $\pm$10 per cent on ξ_2 at fixed D_V with the dotted curves. The scale-dependence of $\Delta\xi_2$ due to the AP effect will allow us to separate the effects of peculiar velocities and the AP effect.

5 ANALYSIS

5.1 Cosmological model space

Given an underlying linear matter power spectrum shape $P_{\rm lin}(k, z_{\rm eff})$, we consider the predicted galaxy clustering as a function of five parameters: $\boldsymbol{p}_{\rm gal} = \{b\sigma_8, f\sigma_8, \sigma_{\rm FoG}^2, (1+z_{\rm eff})D_{\rm A}(z_{\rm eff}), H(z_{\rm eff})\}$. Since the normalization of $P_{\rm lin}(k, z_{\rm eff})$ (denoted throughout as σ_8) determines the amplitude of the second-order perturbation theory corrections in our model, in principle we should be able to separately determine $b\sigma_8$, $f\sigma_8$ and σ_8. In practice, the dependence on σ_8 is sufficiently small and degenerate with the nuisance parameters $b\sigma_8$ and $\sigma_{\rm FoG}^2$ that the degeneracy cannot be broken (see Appendix B3 for details).

We have also assumed that any error in the fiducial cosmological model used to compute $\xi_{0,2}(s)$ from the CMASS galaxy catalogue can be absorbed in a single scaling of distances, interpreted at the effective redshift of the survey. If the assumed redshift dependence of $(1 + z_{\rm eff})D_{\rm A}(z)$ and $H(z)$ is grossly incorrect, we would expect a difference in the correlation functions computed in separate redshift bins; we see no evidence for this in our tests (Ross et al. 2012).

5.1.1 Prior on the linear matter power spectrum from WMAP7

While the scale dependence of galaxy clustering itself can constrain the shape of the linear matter power spectrum, at present (and certainly with the imminent public release of *Planck* data) the constraints enabled by CMB measurements are stronger. The strong CMB constraints mean we can use the entire linear matter power spectrum as a standard ruler determined by observations of the CMB, rather than only the BAO feature. This approach relies on further cosmological model assumptions that are consistent with the current data, but from which moderate deviations are still allowed.

The temperature of the CMB has been measured exquisitely well (Mather et al. 1994), and determines the physical energy density in radiation, $\Omega_r h^2$. In the minimal cosmological model allowed by current observations (Larson et al. 2011), namely a flat ΛCDM cosmology with nearly scale-invariant scalar, adiabatic, Gaussian fluctuations along with the three standard, nearly massless neutrino species, only three additional parameters determine the shape of the underlying linear matter power spectrum, $P_{\rm lin}(k)$. Relative peak heights in the CMB determine the physical energy densities in cold and baryonic matter, $\Omega_{\rm c,b} h^2$, and the overall scale-dependence of the CMB power spectrum determines the spectral index $n_{\rm s}$ of the

nearly scale-invariant scalar primordial fluctuations. Constraints on these parameters do not rely on the distance to the CMB, and thus are immune to the behaviour of dark energy at lower redshifts than the last scattering surface. Moreover, small-scale CMB experiments (Keisler et al. 2011; Hlozek et al. 2012) now probe fluctuations on the same scales as galaxy clustering measurements, and find no compelling evidence for, e.g., a running of the spectral index. Allowing for running of the spectral index would degrade the CMB constraints on the linear matter power spectrum (e.g. Mehta et al. 2012) but we will not include this additional parameter – obviously, our constraints should be interpreted in the context of our model assumptions.

One important extension of the minimal cosmological model is allowing neutrinos to have mass; neutrino oscillation experiments suggest that $\sum m_\nu \gtrsim 0.05$ eV (Abazajian et al. 2011). As the universe expands and cools, massive neutrinos become non-relativistic and modify the linear matter power spectrum inferred from the CMB, as well as alter the expansion history as compared with the massless neutrino case. In this work we ignore this additional uncertainty in the shape of $P_{\rm lin}(k)$. Current upper bounds that combine several cosmological probes find $\sum m_\nu \lesssim 0.3$ eV (e.g. Reid et al. 2010a; de Putter et al. 2012), which is safely below the detectable level in the DR9 CMASS sample (Sanchez et al. 2012).

As we explore the cosmological constraints available from our data set, we will consider a set of power-spectrum shapes parametrized by $\boldsymbol{p}_{\rm s} = \{\Omega_{\rm b}\,h^2,\,\Omega_{\rm c}\,h^2,\,n_{\rm s}\}$. We will marginalize over parameters $\boldsymbol{p}_{\rm s}$ either by importance resampling (Gilks, Richardson & Spiegelhalter 1996; Lewis & Bridle 2002) the public Monte Carlo Markov Chains for a spatially flat ΛCDM model provided by the *WMAP* collaboration or by approximating the constraints on $\boldsymbol{p}_{\rm s}$ with a three-dimensional Gaussian likelihood. Note that the three-dimensional constraints on linear matter power spectrum parameters are very nearly independent of cosmological model extensions that change the expansion rate only for $z \ll 1000$ (i.e. introducing w or $\Omega_{\rm k}$).

5.2 Models

In the present paper, we interpret the anisotropic clustering of CMASS galaxies only in the context of the ΛCDM cosmology. By relaxing assumptions about the redshift–distance relation and/or the growth of structure in the ΛCDM model, we report the statistical precision with which CMASS measurements constrain both the peculiar velocity field $f\sigma_8(z_{\rm eff})$ and geometric quantities $D_{\rm A}(z_{\rm eff})$ and $H(z_{\rm eff})$, without adopting a particular cosmological model that specifies how these quantities are related. We consider the following four models:

(i) *Model 1: WMAP7+CMASS flat ΛCDM.* In the flat ΛCDM cosmology, $f\sigma_8(z_{\rm eff})$, $D_{\rm A}(z_{\rm eff})$ and $H(z_{\rm eff})$ are all determined once $\Omega_{\rm m}$, σ_8 and H_0 are specified. This provides a null test of our assumptions relating CMB fluctuations to predicted galaxy fluctuations.

(ii) *Model 2 WMAP7+CMASS ΛCDM geometry, free growth.* The analysis for this model is the same as Model 1, except that we consider $f\sigma_8$ a free parameter in the CMASS galaxy clustering fits.

(iii) *Model 3 WMAP7+CMASS ΛCDM growth, free geometry.* The analysis for this model is the same as Model 1, except that we consider $D_{\rm A}(z_{\rm eff})$ and $H(z_{\rm eff})$ as free parameters in the CMASS galaxy clustering fits.

(iv) *Model 4 WMAP7+CMASS, free growth, free geometry.* In this model, $f\sigma_8(z_{\rm eff})$, $D_{\rm A}(z_{\rm eff})$ and $H(z_{\rm eff})$ are all free parameters in the fit to the galaxy clustering data. This allows us to determine

how well our data break the degeneracy between the RSD and AP effects, and to present the constraints originating from the amplitude and scale-dependence of the galaxy quadrupole $\xi_2(s)$ in the most model independent way possible. This multivariate distribution can be used to constrain any model that does not alter the shape of the linear matter power spectrum at $z_{\rm eff}$ from that inferred from the CMB on the relatively large scales of interest here.

In all four scenarios we allow the value of $\sigma_{\rm FoG}^2$ to vary between $0\,{\rm Mpc}^2$ and $40\,{\rm Mpc}^2$ with a flat prior and marginalize over both $\sigma_{\rm FoG}^2$ and $b\sigma_8$ when deriving final results. We detail our methods for sampling the multi-dimensional probability distribution functions of interest in Models 1 through 4 in Appendix C.

This approach to parameter fitting allows our estimates of the growth of structure and geometry to be independent of many model assumptions and can be used to put constraints on more general models of gravity and dark energy. However, they still rely on the standard model in three ways. First, we assume that the processes in the early Universe that were responsible for setting up the linear matter power spectrum at recombination do not change significantly, which is true for the most popular models of modified gravity and dark energy. Secondly, we assume that growth at the level of linear perturbation theory is scale independent between the CMB epoch and the effective redshift of our sample. Thirdly, we use GR to compute the perturbation theory corrections to the galaxy clustering predictions. The perturbation theory corrections are not large, and they are most important on small scales where $\sigma_{\rm FoG}^2$ also becomes important; therefore we cannot strongly constrain the amplitude of the higher-order corrections. Constraints on models with scale-dependent growth should be derived directly from the correlation function measurements and their covariance.

5.3 The meaning of σ_8

We follow the standard convention of denoting the amplitude of the matter power spectrum by σ_8^2, even though we restrict our analysis to scales $s > 25\,h^{-1}$ Mpc, so a different weighted integral over $P(k)$ that is concentrated on larger scales would more accurately reflect our constraints on the growth rate of matter fluctuations. In particular, since $P(k)$ is well-determined for k in Mpc^{-1} (e.g. White 2006), and the BAO scale provides a standard ruler with per-cent-level precision, our data constrain the amplitude of matter fluctuations on scales $\gtrsim 36$ Mpc. In practice, the tight constraints on the shape of $P(k)$ means that differences arising from how one specifies its amplitude are small when computing parameter constraints, as long as h is well-determined in the model. In Model 2, we sample power spectra from the *WMAP* ΛCDM chain, and take the traditional value of σ_8 to relate the model parameter f and the reported constraint $f\sigma_8$. In Model 4, we do not specify a value of h with each sampled power spectrum, so we normalize the power spectra by fixing σ_R, where $R = 8/0.7 = 11.4$ Mpc. For power spectra drawn from *WMAP7* ΛCDM chains, $\sigma_R/\sigma_8 = 0.99 \pm 0.024$; the offset and variance between these parameters are negligible compared to our measurement errors on $f\sigma_8$.

6 RESULTS

In this section we present the results of fitting our analytic model for $\xi_{0,2}(s)$ to the observed galaxy correlation functions. Fig. 7 summarizes our constraints from the shape of the observed angle-averaged correlation function $\xi_0(s)$, while Figs 8 and 9 highlight our parameter constraints from the observed anisotropic galaxy clustering.
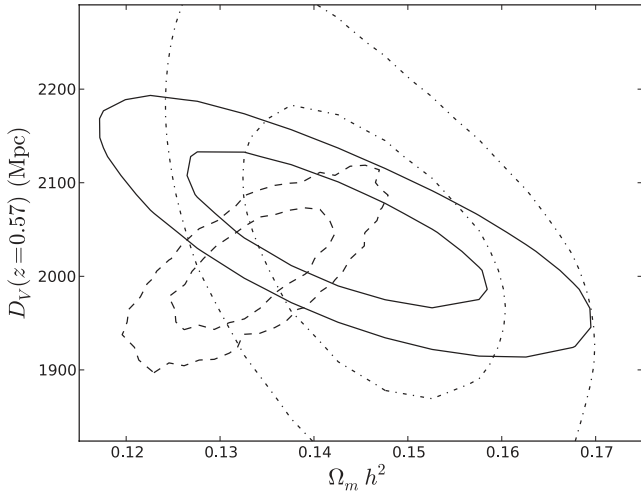
Figure 7. Contours of $\Delta\chi^2 = 2.30$ and 6.17 for fixed $\Omega_b h^2 = 0.02258$ and $n_s = 0.963$ for the monopole ($\ell = 0$) galaxy clustering measurements alone (solid). For comparison, we also compute χ^2 using the 'no-wiggles' power spectrum from Eisenstein & Hu (1998) (dash–dot) to isolate information from the broad-band shape of the correlation function without the BAO feature; this fit is primarily sensitive to the apparent location of the peak in $P(k)$, which corresponds to the horizon size at matter-radiation equality, $\propto \Omega_m h^2 D_V(z_{eff})$. We also project the *WMAP* ΛCDM constraints on to these parameters, and show 68 and 95 per cent contours (dashed).

Constraints on both the peculiar velocity amplitude and geometric quantities $(1 + z_{eff})D_A(z_{eff})$ and $H(z_{eff})$ are summarized in Table 1 for Models 2–4.

### 6.1 Goodness of fit and ΛCDM results

We include 23 separation bins for both $\ell = 0$ and $\ell = 2$ in our χ^2 analyses. In this section, we consider models with increasing numbers of free parameters, and ask whether changes in χ^2 across the models indicate a preference for parameter values outside the predicted values from *WMAP7* in the ΛCDM model. We first fix the underlying power spectrum to the one assumed for all of the mock catalogues, and also fix $\sigma_{FoG}^2 = 21\,\mathrm{Mpc}^2$, the best-fitting value to our *N*-body based mock galaxy catalogues. We vary the galaxy bias, and find a minimum $\chi^2 = 45.7$ for 45 degrees of freedom (DOF),

demonstrating that the mock galaxy catalogues used to validate our model and compute our covariance matrix are consistent with the observed galaxy clustering. If we allow σ_{FoG}^2 to vary as well, $\chi^2 = 42.1$ at $\sigma_{FoG}^2 = 40\,\mathrm{Mpc}^2$. This small difference indicates that we cannot expect a strong constraint on σ_{FoG}^2 within our prior when other cosmological parameters are varying; it is important, however, to marginalize over this nuisance parameter, since it increases our uncertainty in $f\sigma_8$; see the discussion in Section 6.6.

If we restrict ourselves to ΛCDM models consistent with *WMAP7* (Model 1), we find a minimum χ^2 value of 39.3 at $\Omega_m h^2 = 0.1395$ and $H_0 = 68.0\,\mathrm{km\,s^{-1}\,Mpc^{-1}}$ when $b\sigma_8$ and σ_{FoG}^2 are varied. Model 4 has the most free parameters: five describing the galaxy clustering and three specifying the linear matter power spectrum. In this case we find a minimum χ^2 of 39.0 for 41 DOF. This best-fitting model is shown with our measurements of the correlation function in Figs 3 and 4, and has parameter values $b\sigma_8 = 1.235$, $f\sigma_8 = 0.437$, $\sigma_{FoG} = 40\,\mathrm{Mpc}^2$, $D_A = 2184\,\mathrm{Mpc}$, $H = 91.5\,\mathrm{km\,s^{-1}\,Mpc^{-1}}$, $\Omega_m h^2 = 0.1341$, $\Omega_b h^2 = 0.02271$, $n_s = 0.967$. We conclude that the observed $\xi_{0,2}$ is fully consistent with the ΛCDM cosmology; changes in χ^2 values between the models do not indicate a significant preference for parameter values of $f\sigma_8$, F and D_V/r_s outside of the values predicted by *WMAP7* in the ΛCDM model.

CMASS measurements also improve constraints compared to *WMAP7* in the ΛCDM model: $\Omega_m h^2 = 0.1363 \pm 0.0035$, $\Omega_m = 0.283 \pm 0.017$ and $H_0 = (69.3 \pm 1.5)\mathrm{km\,s^{-1}\,Mpc^{-1}}$; *WMAP7* alone finds $\Omega_m h^2 = 0.1334 \pm 0.0056$, $\Omega_m = 0.266 \pm 0.029$ and $H_0 = (71.0 \pm 2.5)\,\mathrm{km\,s^{-1}\,Mpc^{-1}}$. Comparison with the BAO-only results of Anderson et al. (2012) demonstrates that in this minimal model, nearly all of the additional information on these three parameters is coming from the BAO feature.

However, the shape of the measured galaxy correlation function does provide an independent probe of the underlying linear matter power spectrum. With a strong prior on $\Omega_b h^2$ and n_s taken from the CMB, the clustering of galaxies is sensitive to the peak in the linear matter power spectrum, which depends on the horizon size at matter-radiation equality, $\propto \Omega_m h^2$ at fixed effective number of relativistic species ($N_{eff} = 3.04$ for the standard three neutrino species). The scale at which the peak appears depends on the low redshift distance relation, so the broad-band shape of the angle-averaged galaxy power spectrum or correlation function constrains $\Omega_m h^2 D_V(z_{eff})$, in addition to the constraint on $D_V(z_{eff})/r_s(z_{drag})$ that comes from the location of the BAO feature. We illustrate the
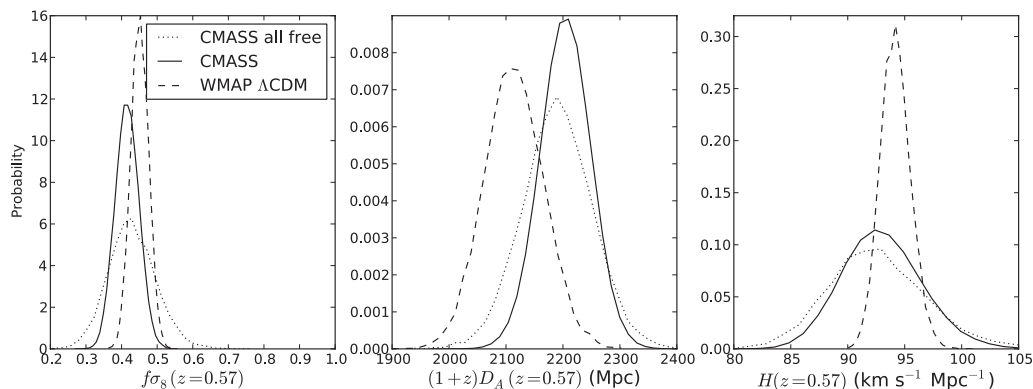
Figure 8. One-dimensional constraints on $f\sigma_8(z_{eff})$, $(1 + z_{eff})D_A(z_{eff})$ and $H(z_{eff})$ under different model assumptions. The dashed curves indicate *WMAP7*-only ΛCDM. The solid (models 2 and 3) and dotted (model 4) curves are constraints derived from the CMASS $\xi_{0,2}$ measurements with a *WMAP7* prior on the underlying linear matter power spectrum $P_{lin}(k/\mathrm{Mpc}^{-1})$. The solid curves additionally use the ΛCDM parameters in the *WMAP7* chains to fix either $(1 + z_{eff})D_A(z_{eff})$ and $H(z_{eff})$, or $f\sigma_8$ (right two panels). All three constraints degrade when fitting for geometry and growth simultaneously using the CMASS observations.
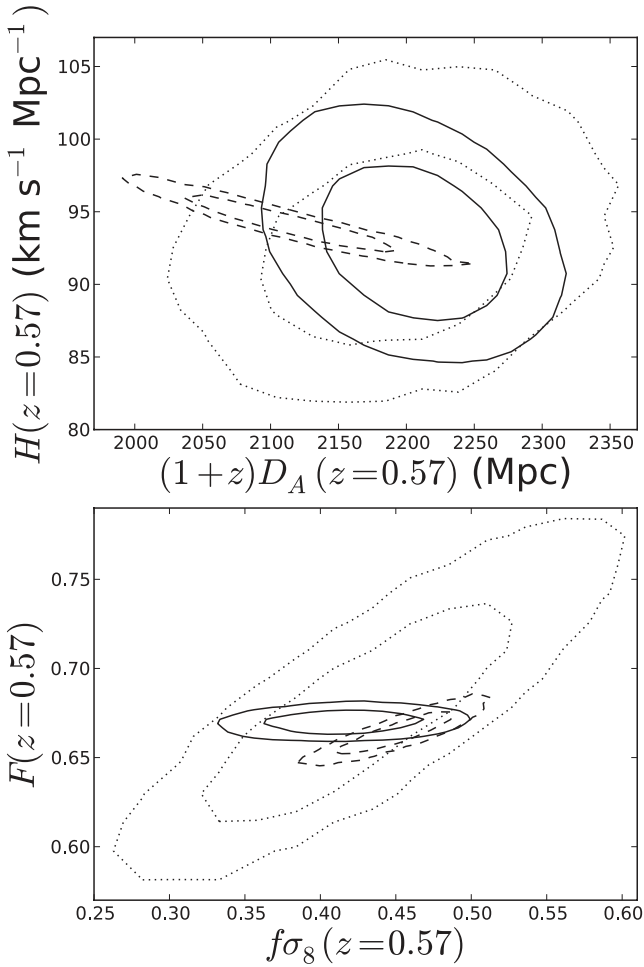
Figure 9. Upper panel: 68 and 95 per cent confidence regions for the co-moving angular diameter distance and expansion rate at $z = 0.57$ from CMASS anisotropic clustering constraints when $f\sigma_8$ is varied over the *WMAP7*+GR flat ΛCDM prior (Model 3; solid) and when $f\sigma_8$ is simultaneously fit (Model 4; dotted). Lower panel: 68 and 95 per cent confidence regions for $f\sigma_8(z = 0.57)$ and AP parameter $F(z = 0.57)$ inferred from CMASS anisotropic clustering (Model 4; dotted). These two parameters are partially degenerate, and their differing scale-dependence allows us to constrain each separately. The solid contour shows the constraint when a *WMAP7*+GR flat ΛCDM prior is used on F. In both panels we show for comparison the predictions from *WMAP7* when a standard GR, flat ΛCDM cosmology is assumed (dashed).

constraining power of our data set by fixing $\Omega_b h^2 = 0.02258$ and $n_s = 0.963$, and computing the CMASS-only likelihood in the $D_V - \Omega_m h^2$ plane shown in Fig. 7 as the solid contours. For this exercise we use only the monopole ($\ell = 0$) measurements, and find a minimum χ^2 value of 18.2 for 19 DOF.

For comparison, we also isolate the broad-band shape information by fitting to a no-wiggle power spectrum (Eisenstein & Hu 1998), which should primarily be sensitive to $\Omega_m h^2 D_V(z_{\text{eff}})$. Results of this fit are shown as dash–dotted contours in Fig. 7. This model provides a poor fit to the measured correlation function, with $\chi^2_{\text{min}} = 38.5$ for 19 DOF, indicating a strong preference for models with the expected BAO feature. However, we do find that the inferred value of $\Omega_m h^2$ from the broad-band shape of the measured galaxy correlation function is consistent with the prediction from the CMB.

Projecting the with-BAO model fits on to $\Omega_m h^2$, we find $\Omega_m h^2 = 0.142 \pm 0.011$. Translating the results of a similar analysis from Reid et al. (2010b) for the SDSS-II LRG sample ($z_{\text{eff}} = 0.31$) to the same assumptions yields $\Omega_m h^2 = 0.141^{+0.010}_{-0.012}$, while the WiggleZ analysis of emission line galaxies at $z_{\text{eff}} \approx 0.6$ finds $\Omega_m h^2 = 0.127 \pm 0.011$ (Blake et al. 2011a). Strictly speaking, these constraints are not uncorrelated since they have a small amount of overlapping volume; neglecting their small correlation, the combined galaxy clustering estimate for $\Omega_m h^2$ is 0.137 ± 0.0064, which marginalizes over the low redshift distance–redshift relation and is in excellent agreement with the *WMAP7* ΛCDM constraint of $\Omega_m h^2 = 0.1334 \pm 0.0056$ (dashed contours in Fig. 7).

6.2 Constraints on the peculiar velocity field amplitude, $f\sigma_8$

In Figs 8 and 9 we compare our constraints on the peculiar velocity field amplitude, $f\sigma_8(z_{\text{eff}})$, from Models 2 (solid) and 4 (dotted) to the predicted distribution from *WMAP7* (dashed), assuming a flat ΛCDM cosmology. The 68 per cent confidence intervals for Models 2 and 4 are listed in Table 1. These measurements agree with the ΛCDM *WMAP7* expectation, 0.451 ± 0.025.

6.3 Geometric constraints

Our tightest geometric constraint comes from the BAO feature in the monopole correlation function. The cosmological parameter dependence of the location of the BAO feature is given by the sound horizon at the drag epoch, $r_s(z_{\text{drag}})$ (we use the definition in Eisenstein & Hu 1998). We find $(D_V(z_{\text{eff}})/r_s(z_{\text{drag}})/(D_V(z_{\text{eff}})/r_s(z_{\text{drag}}))_{\text{fiducial}} = 1.023 \pm 0.019$. The difference between our best-fitting value and the pre-reconstruction fits to the monopole correlation function presented in Anderson et al. (2012) and Sanchez et al. (2012) is due to our different choice of radial binning rather than our fitting methodology; we verified that with the same measurement values and

Table 1. The median and 68.3 per cent confidence level intervals on parameters $b\sigma_8, f\sigma_8$, absolute distance scale D_V (equation 15), AP parameter F (equation 16), as well as derived parameters, comoving angular diameter distance $[(1 + z_{\text{eff}})D_A]$ and expansion rate (H). To obtain these constraints, we marginalize over σ^2_{FoG} and power spectrum shape parameters $p_s = \{\Omega_b h^2, \Omega_c h^2, n_s\}$ for Models 2–4, as described in Section 5.2. We interpret our measurements at the effective redshift of our galaxy sample, $z_{\text{eff}} = 0.57$.

Model	$b\sigma_8$	$f\sigma_8$	D_V (Mpc)	F	$(1 + z_{\text{eff}})D_A$ (Mpc)	H (km s^{-1} Mpc^{-1})
2	$1.228^{+0.033}_{-0.032}$	$0.415^{+0.034}_{-0.033}$	–	–	–	–
3	$1.246^{+0.043}_{-0.046}$	–	2076^{+42}_{-44}	$0.683^{+0.026}_{-0.025}$	2204 ± 44	$92.9^{+3.6}_{-3.3}$
4	$1.238^{+0.047}_{-0.050}$	$0.427^{+0.069}_{-0.063}$	2070^{+43}_{-46}	$0.675^{+0.042}_{-0.038}$	2190 ± 61	$92.4^{+4.5}_{-4.0}$
WMAP7 ΛCDM	–	0.451 ± 0.025	2009 ± 42	$0.6635^{+0.0084}_{-0.0073}$	2113^{+53}_{-52}	$94.2^{+1.4}_{-1.3}$

covariance matrix, our method recovers the same central value as the result presented in Anderson et al. (2012).

Though our fits include information from the broad-band shape of the correlation function, the resulting central value and error on $D_V/r_s(z_{drag})$ are consistent with the fits performed in Anderson et al. (2012), which marginalize over the broad-band shape of correlation function or power spectrum. We therefore conclude that essentially *all* of the information on the distance scale D_V is coming from the BAO feature in the correlation function, as was also true in the analysis of the SDSS-II LRG power spectrum (Reid et al. 2010b). This can be seen in Fig. 7, where at fixed $\Omega_m h^2$, the constraint on D_V is 2.5 times weaker for the 'no-wiggles' fit compared to the fit including the BAO feature. In addition, our central value and error on D_V/r_s are consistent when we fit ξ_0 only, or ξ_0 and ξ_2 simultaneously.

Finally, we note that many of the small differences between the cosmological constraints presented here and those in our companion papers stem from slight differences in the best-fitting value for $D_V/r_s(z_{drag})/(D_V(z_{eff})/r_s(z_{drag}))_{fiducial}$. The correlation function and power spectrum post-reconstruction 'consensus' value from Anderson et al. (2012) is 1.033 ± 0.017; this value was used in cosmological parameter studies in that paper. Sanchez et al. (2012) found 1.015 ± 0.019, in agreement with the pre-reconstruction analysis of the correlation function presented in Anderson et al. (2012).

By combining the *WMAP7* prior on the underlying linear matter power spectrum $\boldsymbol{p}_s$ with information from the AP effect through ξ_2, the standard ruler from the CMB allows us to infer $(1 + z_{eff})D_A(z_{eff})$ and $H(z_{eff})$ separately. Constraints from Model 3 (solid) and Model 4 (dotted) on $(1 + z_{eff})D_A(z_{eff})$ and $H(z_{eff})$ are shown in Figs 8 and 9. Model 3 further uses the *WMAP7* ΛCDM prediction for $f\sigma_8$ to disentangle the RSD and AP effects, and we find factors of 1.3 and 1.2 improvement in $(1 + z_{eff})D_A$ and H errors when adopting this additional assumption: $(1 + z_{eff})D_A = 2204 \pm 44$ (2190 ± 61) Mpc, $H = 92.9^{+3.6}_{-3.3}$ $(92.4^{+4.5}_{-4.0})$ km s^{-1} Mpc^{-1}. In both models, the CMASS distance constraints are consistent with what is inferred from *WMAP7* alone in a ΛCDM cosmology: $(1 + z_{eff})D_A(z_{eff}) = 2113^{+53}_{-52}$ Mpc, $H(z_{eff}) = 94.2^{+1.4}_{-1.3}$ km s^{-1} Mpc^{-1}. We compare the two-dimensional constraints on $(1 + z)D_A$ and H from Models 3 and 4 with the prediction from *WMAP7* for a flat ΛCDM model in Fig. 9, which shows that CMASS constraints on $(1 + z)D_A$ and H are only weakly correlated.

6.4 RSD/AP effect degeneracy

Both quasi-linear peculiar velocities, parametrized by $f\sigma_8(z_{eff})$, and a difference between the assumed and true AP parameter, $F(z_{eff})$, generate a non-zero quadrupole moment in the galaxy correlation function. Fig. 9 shows that while these parameters are positively correlated, our measurements are sufficiently sensitive to distinguish the two through a combination of their differing broad-band scale-dependence and effects on the BAO feature. We quantify this statement further by determining the eigenvectors of the two-by-two marginalized covariance matrix between $f\sigma_8(z_{eff})$ and $F(z_{eff})$ shown in the lower panel of Fig. 9, and projecting those eigenvectors back into $\approx \pm 1\sigma$ changes in ξ_2 around the best-fitting model, shown in Fig. 10. The mode in the upper panel corresponds to the parameter combination constrained to 5 per cent (the minor axis of the dotted ellipse in the bottom panel of Fig. 9), and corresponds mostly to a change in amplitude of the best-fitting ξ_2. The mode in the lower panel is constrained by our measurements to 11 per cent, and contains a change in the slope of ξ_2 on small scales at fixed $\xi_2(s_{min})$ as well as stronger BAO features. To generate these
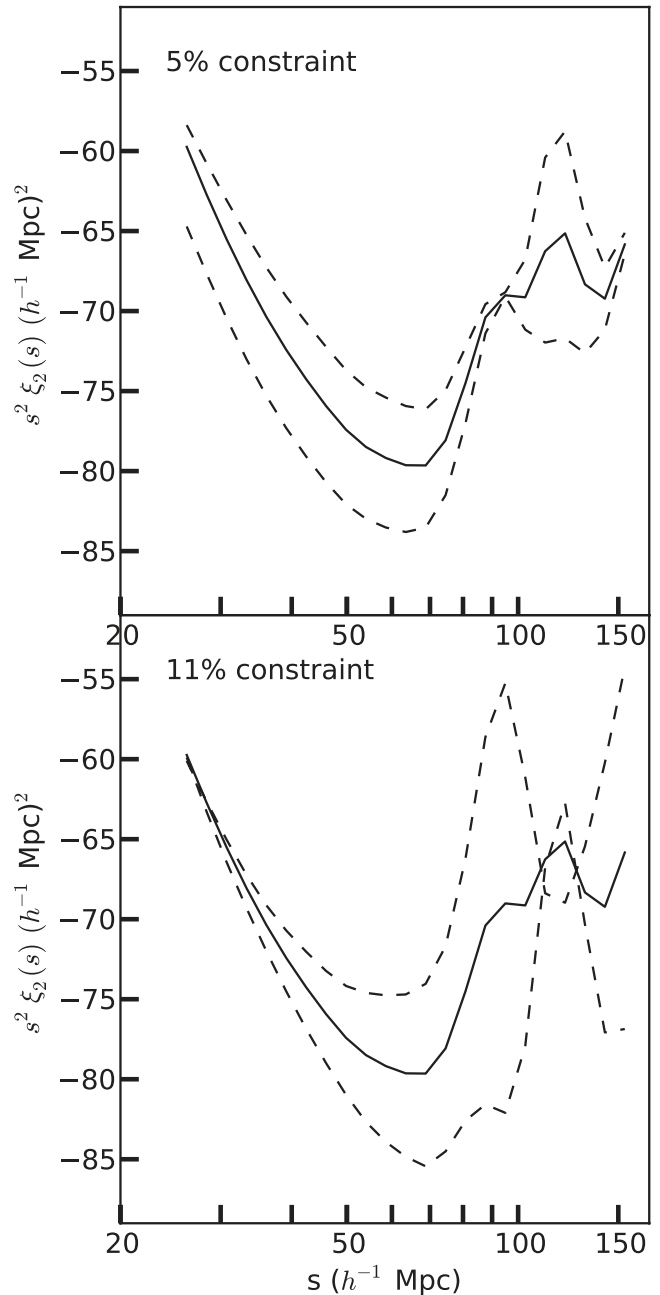
Figure 10. One-sigma changes in ξ_2 about the best-fitting model along the eigenvectors in the marginalized $f\sigma_8 - F$ plane, shown in Fig. 9. In the upper panel we vary $-0.5f\sigma_8 + 0.86F$, which our data constrain to 5 per cent, and in the lower panel we vary $0.86f\sigma_8 + 0.5F$, which our data constrain to 11 per cent. To generate these model curves, $b\sigma_8$, D_V and σ^2_{FOG} were varied to minimize χ^2, so all models shown here predict essentially the same ξ_0.

model predictions, we have minimized χ^2 with respect to $b\sigma_8$, D_V and σ^2_{FOG}. The model ξ_0 (not shown) remains nearly unchanged compared to the best fit.

6.5 Using our results

Our results may be used to test cosmological models which share the assumptions we have adopted in this analysis. Most importantly, we have assumed adiabatic and scale-invariant primordial fluctuations, and that the transfer function was computed assuming the standard

number of massless neutrino species, $N_{eff} = 3.04$. We have assumed that the linear growth is scale-independent, and account for non-linear corrections using perturbation theory within GR. The code to evaluate our theoretical prediction as a function of the underlying linear matter power spectrum, COSMOXI2D, is publicly available.[1] For most purposes, however, our results can be well-approximated by the following multivariate Gaussian likelihood for the parameters $p_{3d} = \{f\sigma_8, F, (D_V/r_s)/(D_V/r_s)_{fiducial}\}$, which should be interpreted at $z_{eff} = 0.57$:

$$\bar{p}_{3d} = \begin{pmatrix} 0.4298 \\ 0.6771 \\ 1.0227 \end{pmatrix} \quad (17)$$

$$10^3 C = \begin{pmatrix} 4.509868 & 2.435891 & -0.01087251 \\ 2.435891 & 1.736087 & -0.06287155 \\ -0.01087251 & -0.06287155 & 0.3548373 \end{pmatrix}. \quad (18)$$

Deviations from the Gaussian likelihood are significant only for points $\gtrsim 3\sigma$ from the best-fitting values, where corrections to the likelihood surface of $\xi_{0,2}$ will also become important.

6.6 Error budget

In this section we examine the main sources of uncertainty in our measurements of the parameters dependent on our measurement of the quadrupole moment $\xi_2(s)$, namely $f\sigma_8(z_{eff})$ and $F(z_{eff})$. We will consider in turn the uncertainty due to the nuisance parameter σ_{FoG}^2 describing the IHV of satellite galaxies (the 'finger-of-God effect'), uncertainty in the underlying linear matter power spectrum, the redshift–distance relation (in the case of peculiar velocities) and the peculiar velocity field (in the case of the AP effect).

We first assess the impact of non-linearity in the covariance matrix on the error budget. Taking the number of galaxies in the present analysis, assuming $\bar{n} = 3 \times 10^{-4} \ (h^{-1} \text{Mpc})^{-3}$, and using linear theory to evaluate the Fisher matrix (as in Reid & White 2011), we expect an uncertainty on $f\sigma_8$ of ≈ 0.021 when only $b\sigma_8$ and $f\sigma_8$ are freely varied. Using our mock covariance matrix, we find an uncertainty of 0.029 on $f\sigma_8$ at fixed $\sigma_{FoG}^2 = 21 \text{Mpc}^2$ and for $P_{lin}(k)$, D_V and F all fixed at their values in the mock catalogue cosmology. This ~ 40 per cent increase is primarily due to the non-linear/window function corrections to the covariance matrix highlighted in Fig. 5. If we instead use the mock based covariance matrix to fit for both D_V and F, fixing σ_{FoG}^2, $P_{lin}(k)$ and $f\sigma_8$, we find $\sigma_F = 0.019$. These results are summarized in Table 2.

6.6.1 Degeneracy with σ_{FoG}^2

At fixed $P(k)$ and geometric parameters, the Fisher matrix analysis indicates a factor of 2 increase in the $f\sigma_8$ error, to 0.042, when σ_{FoG}^2 is marginalized over without any prior, compared to when it is fixed at $\sigma_{FoG}^2 = 21 \text{Mpc}^2$. The marginalized error on σ_{FoG}^2 in the former case is 14 Mpc^2. Therefore, the hard prior $0 < \sigma_{FoG}^2 < 40 \text{Mpc}^2$ substantially reduces this source of uncertainty. Table 2 indicates an increase of only 15 per cent in the error on $f\sigma_8$, to 0.033, when we marginalize over σ_{FoG}^2 within our hard prior. Similarly, marginalizing over σ_{FoG}^2 increases the error on F from 0.019 to

[1] http://mwhite.berkeley.edu/CosmoXi2D

Table 2. We examine how uncertainty in various quantities entering our analysis impacts the 68 per cent confidence level intervals on parameters $b\sigma_8$, $f\sigma_8$ and F. For comparison, the first two rows show the predictions from a simple linear theory Fisher matrix analysis (as in Reid & White 2011) with $\bar{n} = 3 \times 10^{-4} \ (h^{-1} \text{Mpc})^{-3}$, the number of galaxies in the present analysis, and ignoring all window function effects. When σ_{FoG}^2 is marginalized over for the measurements (but *not* for the Fisher matrix analysis), we maintain a hard prior $0 < \sigma_{FoG}^2 < 40 \text{Mpc}^2$. Uncertainty in the underlying linear $P(k)$ is derived from *WMAP7* data, under the assumptions of Gaussian, adiabatic, power-law initial conditions with $N_{eff} = 3.04$ massless neutrino species. Uncertainty in geometry [$D_V(z_{eff})$ and $F(z_{eff})$] or growth [$f\sigma_8$] is taken to be the uncertainty on these quantities derived from *WMAP7* in a ΛCDM cosmology. The last column highlights the cases corresponding to Models 2 though 4.

Marginalized parameters	$\sigma_{b\sigma_8}$	$\sigma_{f\sigma_8}$	σ_F	Model
Fisher	0.019	0.021	–	–
Fisher, σ_{FoG}^2	0.024	0.042	–	–
–	0.023	0.029	–	–
σ_{FoG}^2	0.025	0.033	–	–
σ_{FoG}^2, $P(k)$	0.033	0.033	–	–
σ_{FoG}^2, $P(k)$, geometry	0.033	0.034	–	2
–	0.037	–	0.019	–
σ_{FoG}^2	0.038	–	0.022	–
σ_{FoG}^2, $P(k)$	0.046	–	0.022	–
σ_{FoG}^2, $P(k)$, growth	0.046	–	0.026	3
σ_{FoG}^2	0.047	0.069	0.042	–
σ_{FoG}^2, $P(k)$	0.050	0.069	0.042	4

0.022. Therefore, further reduction in the uncertainty on σ_{FoG}^2 with more detailed modelling of the small-scale clustering would only allow a slight reduction in the errors. However, since our fits indicate a slight preference for $\sigma_{FoG}^2 = 40 \text{Mpc}^2$ compared to the fiducial 21 Mpc^2, in future work we will revisit our choice of prior after a re-analysis of small-scale CMASS clustering with a larger data set.

6.6.2 Uncertainty in the underlying linear matter $P(k)$

Of the three parameters defining the shape of the underlying linear matter power spectrum, $P_{lin}(k)$, in our analysis, the uncertainty in $\omega_c = \Omega_c h^2$ is the largest, particularly in the context of the constraining power of the CMASS measurements. For this comparison, we therefore hold $\Omega_b h^2 = 0.02258$ and $n_s = 0.963$ fixed, and examine how the central values and uncertainties in $b\sigma_8$, $f\sigma_8$ or F change as a function of ω_c, with all other parameters held fixed. Empirically, the uncertainties on these parameters do not depend much on ω_c. Therefore, we can estimate the impact on the uncertainty in ω_c through the dependence of the central value of parameter p on ω_c, in units of the uncertainty on those quantities:

$$s = \frac{\Delta p / \sigma_p}{\Delta \omega_c / \sigma_{\omega_c}}, \quad (19)$$

where σ_p is the uncertainty at fixed ω_c. For Gaussian probability distribution functions in $P(p|\omega_c)$ and $P(\omega_c)$, the uncertainty on p when marginalized over ω_c is increased by $\sqrt{1 + s^2}$. We find that $s \lesssim 0.1$ for $f\sigma_8$ and $s = 0.13$ for F. Therefore, the current uncertainty in the underlying linear matter $P(k)$ is negligible for the purpose of deriving constraints from the anisotropic clustering of CMASS galaxies. This justifies the use of a fixed power spectrum shape in the WiggleZ analyses of anisotropic clustering (Blake et al. 2011b,c). However, the uncertainty in $P(k)$ does increase the uncertainty in $b\sigma_8$, so applications such as galaxy–galaxy lensing/galaxy

clustering combinations (e.g. Reyes et al. 2010) should marginalize over this additional uncertainty.

6.6.3 Uncertainty in ΛCDM geometry

Table 2 indicates that marginalizing over the uncertainty in the geometric quantities $(1 + z_{\mathrm{eff}})D_A(z_{\mathrm{eff}})$ and $H(z_{\mathrm{eff}})$ [or equivalently, $D_V(z_{\mathrm{eff}})$ and $F(z_{\mathrm{eff}})$] contributes negligibly to the uncertainty in $f\sigma_8$ for *WMAP7* uncertainties when a ΛCDM redshift–distance relation is assumed.

6.6.4 Uncertainty in ΛCDM growth of structure

In the ΛCDM model, *WMAP7* constrains Ω_{m} to $\sim$11 per cent; this translates into a relatively large uncertainty in the predicted growth rate of structure ($f\sigma_8$) of 5.5 per cent. Marginalizing over this uncertainty increases our uncertainty on F from 0.022 to 0.026. Weak lensing (e.g. Munshi et al. 2008) and/or cluster abundances (e.g. Vikhlinin et al. 2009; Rozo et al. 2010) reduce the ΛCDM uncertainty on a combination of σ_8 and Ω_{m} similar to the GR prediction for peculiar velocities, $\sigma_8 \Omega_{\mathrm{m}}^{0.55}$, and thus could potentially be used to reduce the uncertainty on $f\sigma_8$ in the ΛCDM growth scenario. In the present work, we do not explore other data set combinations besides *WMAP7* and CMASS.

6.7 Comparison with previous measurements at z ≈ 0.6

The WiggleZ survey has recently analysed the anisotropic clustering of bright emission line galaxies over a broad redshift range (Blake et al. 2011b,c). Their growth rate constraints assumed a fixed underlying linear matter power spectrum and redshift–distance relation, for which our error is 0.033. With a factor of $\sim$4 fewer galaxies, they achieve comparable precision and good agreement with our central value in their $z = 0.6$ bin: $f\sigma_8(z = 0.6) = 0.43 \pm 0.04$. In their analysis they include modes up to $k_{\mathrm{max}} = 0.3\,h\,\mathrm{Mpc}^{-1}$ and marginalize over a Lorentzian model to account for small-scale non-linearities. We find that the quoted WiggleZ error is in good agreement with our Fisher matrix prediction if we assume $\bar{n} = 2.4 \times 10^{-4}\,(h^{-1}\,\mathrm{Mpc})^{-3}$, $b = 1.1$, $N_{\mathrm{gal}} = 60227$, a Gaussian damping $\sigma_{\mathrm{Gauss}} = 300\,\mathrm{km\,s^{-1}}$ and $s_{\mathrm{min}} = 1.15\pi k_{\mathrm{max}}^{-1} = 12\,h^{-1}\,\mathrm{Mpc}$, i.e. a factor of 2 smaller scale than we have adopted for our analysis. Exploration using the Fisher matrix suggests that the difference in number densities between CMASS and WiggleZ has a negligible impact on the uncertainties, while the lower bias of their sample implies a 15 per cent (10 per cent) improvement at $s_{\mathrm{min}} = 25\,(12)\,h^{-1}\,\mathrm{Mpc}$. By far the dominant difference arises because they are fitting out to $k_{\mathrm{max}} = 0.3\,h\,\mathrm{Mpc}^{-1}$; their error would increase by a factor of 2 if they adopted our minimum scale. Another issue is that our mock covariance matrix, which accounts for both non-linear growth of structure and our complex survey geometry, yields errors 40 per cent larger than our naive Fisher matrix analysis would predict, with the difference between the linear and mock covariance matrices increasing on small scales (for ξ_2). While it is not clear how this difference scales with galaxy bias or depends on survey geometry, the WiggleZ use of linear theory covariance matrices down to much smaller scales could cause their uncertainty to be underestimated.

Another recent WiggleZ analysis (Blake et al. 2011c) simultaneously fits $F = 0.68 \pm 0.06$ and $f\sigma_8 = 0.37 \pm 0.08$ at $z = 0.6$ for a fixed underlying $P(k)$, and makes use of modes with $k < 0.2\,h\,\mathrm{Mpc}^{-1}$, which can be compared with the last two lines of Table 2 and Model 4 in Table 1. As in the previous discussion, our

best-fitting values for these parameters are consistent, and using clustering information on small scales (i.e. larger k_{max}) permits a factor of $\sim$1.4 tighter constraint on F at a fixed number of galaxy spectra compared with our clustering analysis of CMASS galaxies. However, the higher bias of CMASS galaxies permits relatively tighter constraints on F than $f\sigma_8$ as compared with WiggleZ.

The WiggleZ and BOSS CMASS surveys target very different galaxy types, which will have different non-linear properties and modelling uncertainties. Without a detailed study it is impossible to understand the robustness of various assumptions for the non-linear distortions, particularly when multiple sources of non-linearity contribute. These can potentially cancel when examining clustering, meaning that goodness-of-fit must be used carefully when assessing robustness and potential biases in a model fit. In this work we have adopted a conservative approach based on the best model available that has been compared with a large volume of *N*-body mock galaxy catalogues, and only fit over those scales where we are confident that the signal is dominated by the quasi-linear velocity field of interest, and where the impact of small-scale random motions can be simply modelled and marginalized over.

7 DISCUSSION

We have analysed the anisotropic clustering of BOSS DR9 CMASS galaxies with an accurate analytic model for the monopole and quadrupole correlation functions, which we have validated using a large volume of *N*-body based mock galaxy catalogues. The combination of the BAO standard ruler and the AP effect allows us to separately constrain the comoving angular diameter distance and Hubble expansion rate at the effective redshift of our sample, $z = 0.57$, while RSDs allow us to constrain the amplitude of the peculiar velocity field, a direct measurement of the growth *rate* of structure, $\mathrm{d}\sigma_8/\mathrm{d}\ln a$. Table 1 summarizes our constraints under several assumptions. Fig. 9 shows the degeneracy between the AP parameter F and the growth rate of structure in our measurements; this explains why our constraints improve considerably if we make further model assumptions about the geometry or growth. In the most general case where all three parameters vary independently, we find $\mathrm{d}\sigma_8/\mathrm{d}\ln a = 0.43^{+0.069}_{-0.063}$, $(1 + z_{\mathrm{eff}})D_A(z_{\mathrm{eff}}) = 2190 \pm 61\,\mathrm{Mpc}$ and $H(z_{\mathrm{eff}}) = 92.4^{+4.5}_{-4.0}\,\mathrm{km\,s^{-1}\,Mpc^{-1}}$.

To illustrate the cosmological constraining power of our measurements, we summarize our results as three distinct tests of a minimal ΛCDM cosmology (defined in Section 5.1) that link the observed CMB anisotropies at $z \approx 1091$ and CMASS galaxy fluctuations at $z \approx 0.57$, independent of the expansion history and growth of structure in the Universe at redshifts below our sample ($z \lesssim 0.57$). We use a flat ΛCDM model to illustrate our constraining power on the behaviour of the Universe at $z > 0.57$, and explore more general cosmological models in our companion paper, Samushia et al. (2012b).

Is the shape of the power spectrum of matter density fluctuations inferred from the CMB consistent with the one inferred from galaxy fluctuations after a factor of ~4 × 10⁵ amplification?

If the dominant component of the energy density is 'cold', then in the linear regime perturbation growth in GR is scale-independent. Modulo our corrections for non-linear ΛCDM evolution and galaxy biasing ($\sim$10 per cent on the scales we analyse), the shapes of the linear matter power spectrum inferred from the CMB and galaxy clustering are consistent: our best-fitting ΛCDM model gives $\chi^2 = 39.3$ for 44 DOF. We quantify this statement further using our fit to the location of the broad turnover in $P(k)$, which indicates the
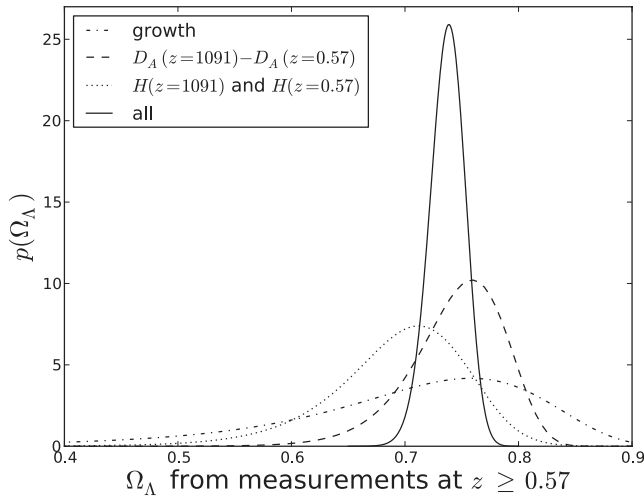
Figure 11. Joint constraints on Ω_Λ from the combination of CMB distance and normalization priors and our measurements of D_A, H and $f\sigma_8$. These constraints are independent of the growth and expansion history at redshifts lower than our galaxy sample, but assume a flat ΛCDM cosmology between the CMASS sample and the CMB, as well as the other model assumptions detailed in Section 5.1.

horizon size at matter–radiation equality and thus the physical matter density, assuming the radiation density is known. Combining our constraint ($\Omega_m h^2 = 0.142 \pm 0.011$) with those in the literature for the SDSS-II LRG sample and WiggleZ yields $\Omega_m h^2 = 0.137 \pm 0.0064$, where the error neglects the expected small but non-zero covariance between the galaxy samples, and also fixes $\Omega_b h^2$ and n_s to best-fitting CMB values. The CMB constraint is only slightly more precise than the combined galaxy measurement ($\Omega_m h^2 = 0.1334 \pm 0.0056$), and the two are in excellent agreement. With this test passed, in the rest of our analysis we make use of the full matter power spectrum (rather than just the BAO feature) as a standard ruler in galaxy clustering measurements. See Sanchez et al. (2012) for an exploration of other cosmological models using the CMASS monopole correlation function shape. In particular, the good agreement between constraints on the linear matter power spectrum from the CMB and CMASS galaxy clustering limits the allowed contribution from species such as massive neutrinos which induce scale-dependent growth.

Do our constraints on the geometry of the Universe require dark energy at $z \gtrsim 0.57$?

Distance constraints from both the CMB and the BAO feature are determined relative to the sound horizon at $z_\star \approx 1091$, the redshift of decoupling, and at $z_{drag} \approx 1020$, the redshift when baryons were released from the Compton drag of the photons.[2] Within the constraints of our cosmological model assumptions (see Section 5.1), $r_s(z_\star)$ and $r_s(z_{drag})$ depend only on $\Omega_m h^2$ and $\Omega_b h^2$. We project the observed *difference* in comoving angular diameter distance $\Delta D_A = (1 + 1091)D_A(z=1091) - (1 + 0.57)D_A(z=0.57)$,

$$\Delta D_A = \int_{0.57}^{1091} \frac{dz}{H(z)} \qquad (20)$$

on to the parameter Ω_Λ in a flat ΛCDM cosmology and marginalize over the other parameters. The result is shown by the dashed line in Fig. 11: $\Omega_\Lambda = 0.76 \pm 0.04$. We quote the maximum likelihood and

---

[2] We follow the *WMAP7* analysis and adopt the fitting formulae for $z_\star$ and z_{drag} from Hu & Sugiyama (1996) and Eisenstein & Hu (1998), respectively.

68 per cent confidence region around it unless otherwise noted. We have purposely chosen a variable that is independent of the expansion history at $z < 0.57$. Similarly, the CMB constraint on $\Omega_m h^2$ with our measurement of $H(z = 0.57)$ requires $\Omega_\Lambda = 0.71^{+0.06}_{-0.05}$ between $z = 0.57$ and $z = 1091$ (dotted curve in Fig. 11).

Does the observed growth rate of structure at $z = 0.57$ require dark energy?

Because *WMAP* places such a tight constraint on the amplitude of curvature perturbations deep in the matter-dominated epoch at $k = 0.027\,\mathrm{Mpc}^{-1}$ (1.8 per cent), we can translate our measurement of $f\sigma_8$ into a constraint on $dD/d\ln a$, where D is the usual growth function that depends only on Ω_m or Ω_Λ in a flat ΛCDM cosmological model:

$$D(z) = \frac{5\Omega_m}{2} \frac{H(z)}{H_0} \int_{}^{1/(1+z)} \frac{da\,H_0^3}{[a\,H(a)]^3}. \qquad (21)$$

To do so, we require the additional cosmological model assumptions listed in Section 5.1. We marginalize over the *WMAP7* uncertainties in the parameters that convert curvature perturbations to the integrated amplitude of matter perturbations on scales of $R = 8/0.7 = 11.4\,\mathrm{Mpc}$, σ_R, namely $\Omega_m h^2$, $\Omega_b h^2$ and n_s. Section 5.3 details the relation between σ_R and σ_8, which can be regarded as equal for our purposes. This comparison between the fluctuation amplitude at $z = 1091$ and $z = 0.57$ requires Ω_Λ within [0.59, 0.81] (central 68 per cent confidence), with a maximum likelihood at 0.76. The distribution is shown as the dot–dashed curve in Fig. 11.

In combination with the CMB, both our geometric and growth rate constraints require a value of Ω_Λ at $0.57 < z < 1091$ that is consistent with the concordance model expectation. Combining all three constraints with the *WMAP7* distance and normalization priors, and marginalizing over $\Omega_b h^2$ and $\Omega_m h^2$, we find $\Omega_\Lambda = 0.74^{0.016}_{-0.015}$ (solid curve in Fig. 11).

Our analysis required further assumptions compared with a BAO-only analysis (Anderson et al. 2012) that constrains $D_V(z_{eff})/r_s(z_{drag})$. However, we were able to perform tests of the scale-independence and growth rate of cosmic structure between recombination and $z \approx 0.57$, as well as to break the degeneracy between $(1 + z_{eff})D_A$ and H using the AP test. So far, our measurements do not unveil any deviations from the minimal ΛCDM model we have examined. Under the assumption of a ΛCDM cosmology extending to $z = 0$, the BAO feature adds the most constraining power to *WMAP7* on ΛCDM parameters; we find $\Omega_m h^2 = 0.1363 \pm 0.0035$, $\Omega_m = 0.283 \pm 0.017$ and $H_0 = 69.3 \pm 1.5\,\mathrm{km\,s}^{-1}\,\mathrm{Mpc}^{-1}$ in this model. We anticipate statistical improvements on these results with the completed BOSS galaxy data set covering a footprint three times larger, as well as developments in the theoretical modelling that will allow tighter cosmological constraints.

REFERENCES

Abazajian K. et al., 2011, Astropart. Phys., 35, 177
Ade P. et al., 2011, A&A, 536, A1
Ahn C. et al., 2012, ApJS, preprint (arXiv:1207.7137)
Alcock C., Paczynski B., 1979, Nat, 281, 358
Allen S., Evrard A., Mantz A., 2011, ARA&A, 49, 409
Amanullah R. et al., 2010, ApJ, 716, 712
Anderson L. et al., 2012, MNRAS, preprint (arXiv:1203.6594)
Ballinger W., Peacock J., Heavens A., 1996, MNRAS, 282, 877
Beutler F. et al., 2011, MNRAS, 416, 3017
Blake C., Collister A., Bridle S., Lahav O., 2007, MNRAS, 374, 1527
Blake C. et al., 2011a, MNRAS, 418, 1707
Blake C. et al., 2011b, MNRAS, 415, 2876
Blake C. et al., 2011c, MNRAS, 418, 1725
Bolton A. et al., 2012, AJ, preprint (arXiv:1207.7326)
Chuang C., Wang Y., 2012, MNRAS, 426, 226
Cole S., Aragon-Salamanca A., Frenk C. S., Navarro J. F., Zepf S. E., 1994, MNRAS, 271, 781
Cole S., Fisher K., Weinberg D., 1995, MNRAS, 275, 515
Cole S. et al., 2005, MNRAS, 362, 505
Cooray A., Sheth R., 2002, Phys. Rep., 372, 1
da Angela J. et al., 2008, MNRAS, 383, 565
Davis M., Huchra J., 1982, ApJ, 254, 437
Dawson K. et al., 2012, preprint (arXiv:1208.0022)
de Putter R. et al., 2012, preprint (arXiv:1201.1909)
Diaferio A., Geller M., 1996, ApJ, 467, 19
Drinkwater M. et al., 2010, MNRAS, 401, 1429
Eisenstein D. J., Hu W., 1998, ApJ, 511, 5
Eisenstein D. J., White M., 2004, Phys. Rev. D, 70, 103523
Eisenstein D. J. et al., 2005, ApJ, 633, 560
Eisenstein D. J. et al., 2011, AJ, 142, 72
Fisher K. B., 1995, ApJ, 448, 494
Fukugita M., Ichikawa T., Gunn J., Doi M., Shimasaku K., Schneider D., 1996, AJ, 111, 1748
Gaztanaga E., Cabre A., Hui L., 2009, MNRAS, 399, 1663
Gilks W. R., Richardson S. R., Spiegelhalter D. J., eds, 1996, Markov Chain Monte Carlo in Practice. Chapman & Hall, Florida
Gunn J. E. et al., 1998, AJ, 116, 3040
Gunn J. E. et al., 2006, AJ, 131, 2332
Guo H., Zehavi I., Zheng Z., 2011, preprint (arXiv:1111.6598)
Guzzo L. et al., 2008, Nat, 451, 541
Hamilton A., 1992, ApJ, 385, L5
Hamilton A., 1993, ApJ, 417, 19
Hamilton A. J. S., 1998, in Hamilton D., ed., Linear Redshift Distortions: A Review. The Evolving Universe. Kluwer, Dordrecht, p. 185
Hlozek R. et al., 2012, ApJ, 749, 90
Hu W., Sugiyama N., 1996, ApJ, 471, 542
Hütsi G., 2006, A&A, 449, 891
Jain B., Zhang P., 2008, Phys. Rev. D, 78, 063503
Kaiser N., 1987, MNRAS, 227, 1
Kauffmann G., White S. D. M., Guiderdoni B., 1993, MNRAS, 264, 201
Kazin E. et al., 2010, ApJ, 710, 1444
Kazin E., Sanchez A., Blanton M., 2011, MNRAS, 419, 3223
Keisler R. et al., 2011, ApJ, 743, 28
Kessler R. et al., 2009, ApJS, 185, 32
Komatsu E. et al., 2011, ApJS, 192, 18
Kravtsov A., Berlind A., Wechsler R., Klypin A., Gottlöber S., Allgood B., Primack J., 2004, ApJ, 609, 35
Landy S. D., Szalay A. S., 1993, ApJ, 412, 64
Larson D. et al., 2011, ApJS, 192, 16
Lewis A., Bridle S., 2002, Phys. Rev. D., 66, 103511
McDonald P., Seljak U., 2009, J. Cosmol. Astropart. Phys., 10, 7
Manera M. et al., 2012, MNRAS, preprint (arXiv:1203.6609)
Maraston C. et al., 2012, MNRAS, preprint (arXiv:1207.6114)
Masters K. et al., 2011, MNRAS, 418, 1055
Mather J. et al., 1994, ApJ, 420, 439
Matsubara T., 2008, Phys. Rev. D., 78, 083519
Matsubara T., Suto Y., 1996, ApJ, 470, L1
Mehta K., Seo H.-J., Eckel J., Eisenstein D. J., Metchnik M., Pinto P., Xu X., 2011, ApJ, 734, 94
Mehta K., Cuesta A., Xu X., Eisenstein D. J., Padmanabhan N., 2012, preprint (arXiv:1202.0092)
Munshi D., Valageas P., van Waerbeke L., Heavens A., 2008, Phys. Rep., 462, 67
Nesseris S., Perivolaropoulos L., 2008, Phys. Rev. D, 77, 023504
Okumura T., Matsubara T., Eisenstein D., Kayo I., Hikage C., Szalay A., Schneider D., 2008, ApJ, 676, 889
Padmanabhan N., White M., 2008, Phys. Rev. D, 77, 123540
Padmanabhan N., White M., 2009, Phys. Rev. D, 80, 063508
Padmanabhan N. et al., 2007, MNRAS, 378, 852
Papai P., Szapudi I., 2008, MNRAS, 389, 292
Peacock J. A. et al., 2001, Nat, 410, 169
Percival W. J., White M., 2008, MNRAS, 393, 297
Percival W. J. et al., 2004, MNRAS, 353, 1201
Percival W., Cole S., Eisenstein D., Nichol R., Peacock J., Pope A., Szalay A., 2007, MNRAS, 381, 1053
Percival W. J. et al., 2010, MNRAS, 401, 2148
Perlmutter S. et al., 1999, ApJ, 517, 565
Reid B. A., White M., 2011, MNRAS, 417, 1913
Reid B. A., Verde L., Jimenez R., Mena O., 2010a, J. Cosmol. Astropart. Phys., 1, 3
Reid B. A. et al., 2010b, MNRAS, 404, 60
Reyes R., Mandelbaum R., Seljak U., Baldauf T., Gunn J. E., Lombriser L., Smith R. E., 2010, Nat, 464, 256
Riess A. et al., 1998, ApJ, 116, 1009
Riess A. et al., 2011, ApJ, 730, 119
Ross A. et al., 2012, MNRAS, 424, 564
Rozo E. et al., 2010, ApJ, 708, 645
Samushia L. et al., 2011, MNRAS, 410, 1993
Samushia L., Pericval W. J., Raccanelli A., 2012a, MNRAS, 420, 2102
Samushia L. et al., 2012b, preprint (arXiv:1206.5309)
Sanchez A. et al., 2012, MNRAS, 425, 415
Schlegel D., White M., Eisenstein D. J., 2009, The Astronomy and Astrophysics Decadal Survey, Science White Papers 314, preprint (arXiv:0902.4680)
Seo H. J. et al., 2010, ApJ, 720, 1650

Skibba R., van den Bosch F., Yang X., More S., Mo H., Fontanot F., 2011, MNRAS, 410, 417

Smee S. et al., 2012, AJ, preprint (arXiv:1208.2233)

Song Y.-S., Koyama K., 2009, J. Cosmol. Astropart. Phys., 1, 48

Song Y.-S., Percival W. J., 2009, J. Cosmol. Astropart. Phys., 10, 4

Song Y. S., Sabiu C. G., Nichol R. C., Miller C. J., 2010, J. Cosmol. Astropart. Phys., 1, 25

Song Y. S., Sabiu C. G., Kayo I., Nichol R. C., 2011, J. Cosmol. Astropart. Phys., 5, 20

Taruya A., Saito S., Nishimichi T., 2011, Phys. Rev. D, 83, 103257

Tegmark M., 1997, Phys. Rev Lett., 79, 3806

Tojeiro R. et al., 2012, MNRAS, 424, 2339

Vikhlinin A. et al., 2009, ApJ, 692, 1060

White M., 2006, New Astron. Rev., 50, 938

White M., Song Y.-S., Percival W., 2009, MNRAS, 397, 1348

White M. et al., 2011, ApJ, 728, 126

Xu X., Padmanabhan N., Eisenstein D., Mehta K., Cuesta A., 2012, preprint (arXiv:1202.0091)

York D. G. et al., 2000, AJ, 120, 1579

Zhao G. B., Giannantonio T., Pogosian L., Silvestri A., Bacon D. J., Koyama K., Nichol R. C., Song Y. S., 2010, Phys. Rev. D, 81, 103510

APPENDIX A: OBSERVATIONAL UNCERTAINTIES

A1 Uncertainties in radial distribution

To compute overdensities of the galaxy field, defined as

$$\delta(z, \hat{\Omega}) = \frac{\rho(z, \hat{\Omega}) - \rho_0(z, \hat{\Omega})}{\rho_0(z, \hat{\Omega})}, \tag{A1}$$

we must know the unperturbed density field $\rho_0(z, \hat{\Omega})$. While the angular selection function of the survey is usually well known, the radial distribution is not easy to model accurately. Usually, the unperturbed radial distribution of galaxies is modelled from the distribution of observed redshifts by either shuffling them or splining with a smooth curve. Different ways of constructing a random catalogue will result in different estimates of correlation function (see e.g. Ross et al. 2012; Samushia et al. 2012a).

To estimate the magnitude of this effect on the measurements of the moments of correlation function we take 600 PTHalos mock catalogues of CMASS sample and apply simplified version of our analysis to the measurements produced using different ways of reconstructing $n(z)$. We reconstruct $n(z)$ first by shuffling 'observed' redshifts in mock catalogues and then by splining that distribution with 10, 20 and 30 node cubic spline fits.

We find that the ways of reconstructing $n(z)$ for random catalogues do not affect the RSD measurements significantly. In our current analysis we are using the 'shuffled' catalogues since they introduce the least bias in the measurements of $\xi_\ell(r)$ (Ross et al. 2012).

A2 Effects of close pairs, redshift errors and redshift failures

We are unable to obtain redshifts for ∼5 per cent of the galaxies due to fibre collisions – no two fibres on any given observation can be placed closer than 62 arcsec. At $z \simeq 0.5$, this 62 arcsec exclusion corresponds to $0.4 \, h^{-1}$ Mpc. Redshifts for some of the collided galaxies can be reclaimed in regions where several plates observe a common patch of the sky, but the remaining exclusion must be accounted for. We account for fibre-collided galaxies by assigning its weight to its nearest neighbour on the sky. Tests on mock catalogues presented in Guo, Zehavi & Zheng (2011) indicate

that the nearest neighbour correction adopted in this work is accurate to better than 1 per cent for both ξ_0 and ξ_2 at the scales used in our analysis.

Redshift failures are discussed in detail in Ross et al. (2012); we also correct for them with a nearest-neighbour upweighting scheme. Redshift measurement errors smooth the apparent galaxy density field, in the same fashion as described with our nuisance parameter $\sigma_{\rm FoG}^2$. The median redshift error for our sample is $42 \, \text{km s}^{-1}$, which translates into an additive contribution to $\sigma_{\rm FoG}^2 < 1 \, \text{Mpc}^2$.

APPENDIX B: ACCURACY AND IMPLEMENTATION OF THE THEORETICAL MODEL

B1 Wide angle effects

Equations (10) and (12) assume that a 'plane-parallel' approximation, which states that the sample is far enough from the observer so that all LOSs are parallel to each other, is accurate enough. This approximation will fail at some scale for wide surveys (see e.g. Papai & Szapudi 2008). We approximate the scale-dependent magnitude of wide-angle effects for our sample in a similar manner to Samushia et al. (2012a). The effective redshift of our galaxy sample is $z = 0.57$, which in the best-fitting *WMAP7* cosmology corresponds to a comoving distance of approximately $1500 \, h^{-1}$ Mpc. The largest scale that we consider in this analysis is $160 \, h^{-1}$ Mpc, which corresponds to an opening angle of about $3°$. We estimate the wide-angle corrections to be at most 10 per cent of the statistical errors on the largest scales and do not try to correct for this effect in current analysis.

B2 COSMOXI2D code implementation

Reid & White (2011) demonstrated that equation (12) provides an accurate description of $\xi_{\rm g}^s(r_\sigma, r_\pi)$ when real space clustering and velocity statistics inside the integrand are measured directly from N-body simulations. Moreover, in the regime where $1 + b_{1L} = b \approx 2$ (appropriate for CMASS galaxies), the real space clustering and velocity statistics can be computed analytically with sufficient precision to predict $\xi_{\rm g}^s(r_\sigma, r_\pi)$. In detail, this 'sweet spot' in the precision of the model arises because the functions $v_{12}(r)$ and $\sigma_{12,\parallel/\perp}^2(r)$ entering equation (12) were evaluated as a function of cosmological parameters in standard perturbation theory accounting for only the linear bias of the tracer. At the redshift of interest, the second order Lagrangian bias b_{2L} crosses zero near $1 + b_{1L} = 2$, and the calculation of these functions neglecting b_{2L} is sufficient for our purposes. We therefore caution against the use of our code for tracers with bias substantially different from 2. Note that $\xi_{\rm g}^r(r)$ is evaluated in LPT (Matsubara 2008) and includes the contribution to the real space clustering from second-order Lagrangian bias.[3]

Standard perturbation theory is known to have inaccuracies in describing the BAO feature, and we found that on BAO scales errors in our perturbation theory calculation of pairwise velocity statistics caused inaccuracies in the prediction for $\xi_{\rm g}^s(r_\sigma, r_\pi)$. However, on scales $s \gtrsim 70 \, h^{-1}$ Mpc, the redshift space version of LPT (Matsubara 2008) is very accurate (see fig. 2 of Reid & White 2011). We therefore interpolate between our evaluation of equation (12) at

---

[3] We relate the second-order Lagrangian bias, b_{2L}, to the first-order bias, b_{1L}, through the peak background split; these parameters are not varied independently.

smaller scales and LPT on large scales, with the transition fixed at 100 Mpc.

Finally, we model the effect of galaxy IHV (traditional 'fingers-of-God') by convolving our model $\xi(r_p, r_\pi)$ with an additional Gaussian velocity dispersion of variance σ_{FoG}^2. Using the Gaussian form allows σ_{FoG}^2 to be included directly in the Gaussian in equation (12) for faster evaluation of our model as we explore cosmological parameter space.

We have developed a code to numerically evaluate equation (12) as well as all the relevant perturbation theory integrals as a function of an input linear matter power spectrum and nuisance parameters b and σ_{FoG}^2. The AP effect is easily incorporated using equation (13) before computing Legendre polynomial moments from $\xi_g^s(r_\sigma, r_\pi)$. The internal units of COSMOXI2D are Mpc, in which the underlying linear matter power spectrum is most tightly constrained. The code is publicly available.[4]

B3 Model accuracy

Because we have such a large volume of simulations, we can use the difference between the theoretical model at the known cosmological parameters of the N-body simulation and the measured correlation function from the mock galaxy catalogues to quantify our theoretical systematic error; we find $\Delta\chi^2 = 0.29$ at the best-fitting value of σ_{FoG}^2. We also compare the scale dependence of the model error with the five parameters p_{gal} we are fitting, and find $<0.25\sigma$ shifts compared to the *unmarginalized* uncertainties on all parameters (i.e. the uncertainty on each parameter if all the others were known perfectly). Therefore we conclude that our systematic error is negligible in the context of this analysis.

Another concern is that the model becomes inaccurate rapidly on scales smaller than our minimum fitting scale, s_{min}. When AP parameters vary, scales smaller than s_{min} contribute to the model. However, we have verified that for variations of 10 per cent in D_V and/or 20 per cent in F (i.e. much larger than the final uncertainties), the theoretical error induces $<0.5\sigma$ shifts in all parameters compared with the unmarginalized uncertainties.

Finally, we point out that unlike in linear theory, our model depends on b, f and σ_8 separately, rather than only the combinations $b\sigma_8$ and $f\sigma_8$. However, at the particular $b\sigma_8$ and $f\sigma_8$ values of our sample, we find that changes in the predicted $\xi_{0,2}$ with σ_8 can be absorbed by changes in the value of $b\sigma_8$. Quantitatively, for a ±10 per cent change in away from our fiducial $\sigma_8(z_{\text{eff}}) = 0.61$ and at fixed $P(k)$, AP parameters, and $\sigma_{\text{FoG}}^2 = 21$ Mpc^2, $b\sigma_8$ shifts by $\approx\pm1.3\sigma$ with no measurable shift in the central value of $f\sigma_8$.

B4 Propagating uncertainties in the galaxy–halo mapping to σ_{FoG}^2

As shown in Fig. 6, our model with $\sigma_{\text{FoG}}^2 = 21$ Mpc^2 fits the $\xi_{0,2}(s)$ of our mock galaxy catalogues, based on the best-fitting HOD in White et al. (2011). In this section we quantify how uncertainties in both the theoretical modelling and data analysis cause uncertainty in the expected value of σ_{FoG}^2 for the CMASS sample. We address several aspects of this problem separately.

(i) *One-halo versus two-halo contributions to $\xi_{0,2}$ and fibre collision corrections*. The formalism of the halo model distinguishes between 'one-halo' and 'two-halo' pairs depending on whether the two galaxies occupy the same or different haloes. In Fig. B1 we show

[4] http://mwhite.berkeley.edu/CosmoXi2D
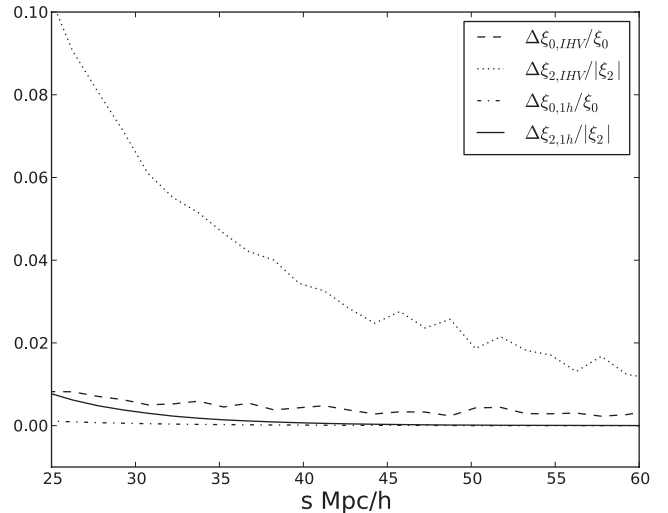
Figure B1. The dashed (dotted) lines show the fractional change in ξ_0 (ξ_2) in our mock galaxy catalogues due to satellite galaxy IHV (also shown in Fig. 6). We isolate the contribution of pairs of galaxies occupying the same halo in our mock catalogues (i.e. 'fingers-of-God'), shown as the dot–dashed (solid) curves for ξ_0 (ξ_2). On the scales of interest, the dominant effect of IHV is a net diffusion of pairs from small scales (where ξ is larger) to larger scales.

the total change in $\xi_{0,2}$ due to satellite galaxy IHV by the dashed (dotted) curves in our mock catalogues. The dash–dotted and solid curves show the contributions to this change in $\xi_{0,2}$ from one-halo pairs, which are localized along the LOS with $r_\sigma \lesssim 1\,h^{-1}$ Mpc. Because the one-halo pairs contribute to such a small $d\mu$, they can be neglected on the scales used in our cosmological parameter fits, $s \geq 25\,h^{-1}$ Mpc. This fact is important to establish since our method for fibre collision corrections will correctly recover the distribution of pair separations for pairs of galaxies with separations larger than the fibre collision scale, but suppresses the contribution of pairs of galaxies at the fibre collision scale ($r_\sigma \lesssim 0.5\,h^{-1}$ Mpc).

(ii) *Uncertainty in the HOD at fixed cosmology*. Uncertainties in the HOD parameters will introduce an uncertainty in σ_{FoG}^2. While σ_{FoG}^2 is roughly proportional to the satellite fraction, it also depends on the distribution of host halo mass – increasing α and κ increases host halo mass at fixed satellite fraction, which increases σ_{FoG}^2. We use Markov chain Monte Carlo (MCMC) chains from White et al. (2011) to estimate our uncertainty on σ_{FoG}^2 at fixed cosmology to be 6 Mpc^2.

(iii) *Breakdown of the 'central' galaxy assumption*. The analysis of Skibba et al. (2011) suggests that the brightest galaxy in a halo is not always the 'central' one. We test the impact of relaxing our assumption that the velocity of mock central galaxies has no IHV by assigning them the intrahalo velocity of a random dark matter particle halo member in our simulations some fraction p of the time. When the number of galaxies in a halo N_{gal} is larger than one, we assume that the chance of not including the 'central' galaxy in our sample is lower, $\propto p^{N_{\text{gal}}}$. For $p = 0.3$, we find σ_{FoG}^2 at our fiducial HOD is increased by 9 Mpc^2.

(iv) *Variations in the halo mass function with cosmological parameters*. A broad range of observations show good agreement between the concordance ΛCDM halo mass function and the multiplicity of galaxy groups and clusters (e.g. Rozo et al. 2010; Allen, Evrard & Mantz 2011), so this uncertainty is subdominant: even if our fiducial HOD masses were scaled by a factor of 2, $\sigma_{\text{FoG}}^2 \propto M^{2/3}$ would change by 11 Mpc^2.

Given the above considerations, we adopted a generous hard prior on σ_{FoG}^2 between 0 and 40 Mpc^2.

APPENDIX C: MARKOV CHAIN MONTE CARLO METHODS

We adopt a hybrid MCMC/importance resampling approach to explore the BOSS likelihood surface with various priors imposed from the *WMAP7* likelihood in Models 1–4. This approach is necessary in our case because our model evaluation is slow, and we must marginalize over $b\sigma_8$ and σ_{FoG}^2 at each point in parameter space that we consider. This section describes our methods in each case.

C1 Importance resampling

WMAP7 MCMC chains are publicly available.[5] These chains provide a fair sample of the *WMAP7* likelihood surface. Importance resampling (Gilks et al. 1996; Lewis & Bridle 2002) allows us to compute how constraints on the model parameters change given an additional constraint by evaluating the new likelihood at a subsample of the original MCMC chain, multiplying the original weight of each element by the new likelihood, and then recomputing confidence intervals.

C2 Model 1: *WMAP7*+CMASS ΛCDM

For this model we marginalize only over two parameters, so it is feasible to directly compute a marginalized CMASS likelihood:

$$P_{\mathrm{CMASS}}(\theta_{\Lambda\mathrm{CDM}}) = \int \mathrm{d}b\sigma_8 \, \mathrm{d}\sigma_{\mathrm{FoG}}^2 \, \mathrm{e}^{-\chi_{\mathrm{CMASS}}^2(\theta_{\Lambda\mathrm{CDM}}, b\sigma_8, \sigma_{\mathrm{FoG}}^2)/2}. \quad \text{(C1)}$$

We then use importance resampling of the *WMAP7* chain parameters.

C3 Model 2 *WMAP7*+CMASS ΛCDM geometry, free growth; Model 3 *WMAP7*+CMASS ΛCDM growth, free geometry

In Models 2 and 3, for each linear matter power spectrum, we must vary three or four extra parameters describing the galaxy clustering observations. We therefore explore the likelihood surface at each point in the *WMAP7* chain by MCMC, and thereby sample the CMASS likelihood distribution $P(\theta_{\mathrm{CMASS}}|\theta_{\Lambda\mathrm{CDM}})$. In Model 2, $\theta_{\mathrm{CMASS}} = \{b\sigma_8, \sigma_{\mathrm{FoG}}^2, f\sigma_8\}$, and in Model 3, $\theta_{\mathrm{CMASS}} = \{b\sigma_8, \sigma_{\mathrm{FoG}}^2, D_V, F\}$. MCMC chains at a fixed $\theta_{\Lambda\mathrm{CDM}}$ sample parameter space proportional to $P(\theta_{\mathrm{CMASS}}|\theta_{\Lambda\mathrm{CDM}})$, but in order to compute the marginalized likelihood of $f\sigma_8$ in Model 2 or D_V, F in Model 3, we must determine the relative likelihood of the MCMC chains evaluated at different $\theta_{\Lambda\mathrm{CDM}}$. Since

$$N\mathrm{e}^{-\chi^2(\theta_{\mathrm{CMASS}}, \theta_{\Lambda\mathrm{CDM}})/2} = P(\theta_{\mathrm{CMASS}}, \theta_{\Lambda\mathrm{CDM}})$$
$$= P(\theta_{\mathrm{CMASS}}|\theta_{\Lambda\mathrm{CDM}})P(\theta_{\Lambda\mathrm{CDM}}) \quad \text{(C2)}$$

where N is an overall normalization, we can combine the χ^2 computed at any point with the probability density estimated by our MCMC to determine the relative normalization of $P(\theta_{\Lambda\mathrm{CDM}})$. In practice, we first normalize each MCMC distribution so that $\int P(\theta_{\mathrm{CMASS}}|\theta_{\Lambda\mathrm{CDM}}) = 1$, find $\theta_{\mathrm{CMASS}}^\star(\theta_{\Lambda\mathrm{CDM}})$ with the minimum value of χ^2 in each chain and integrate the normalized $P(\theta_{\mathrm{CMASS}}|\theta_{\Lambda\mathrm{CDM}})$ in a small, fixed size region of parameter space around $\theta_{\mathrm{CMASS}}^\star$, which we call $\tilde{p}(\theta_{\mathrm{CMASS}}^\star, \mathrm{d}\theta_{\mathrm{CMASS}})$.[6] The relative weight of each point in the *WMAP*-only MCMC chain is then determined by the CMASS-only likelihood value and $\tilde{p}$:

$$w(\theta_{\Lambda\mathrm{CDM}}) = \mathrm{e}^{-\chi^2(\theta_{\mathrm{CMASS}}^\star|\theta_{\Lambda\mathrm{CDM}})/2} (\tilde{p}(\theta_{\mathrm{CMASS}}^\star, \mathrm{d}\theta_{\mathrm{CMASS}}))^{-1}. \quad \text{(C3)}$$

We find that our constraints are the same if we neglect this volume weighting factor $\tilde{p}^{-1}$, indicating that the effective volume of parameter space allowed by the CMASS measurements does not strongly depend on the underlying cosmological parameters $\theta_{\Lambda\mathrm{CDM}}$ when exploring the region of this parameter space allowed by *WMAP7*.

C4 Model 4 *WMAP7*+CMASS, free growth, free geometry

In this case, we use *WMAP* data to provide a prior on the shape of the linear matter power spectrum, which is well approximated by a multivariate Gaussian in the parameters $\Omega_{\mathrm{c}} h^2$, $\Omega_{\mathrm{b}} h^2$, n_{s}. *WMAP7* constraints on these parameters primarily come from ratios of peak heights and the overall shape, rather than the locations of the peaks (which are sensitive to the angular diameter distance to the last scattering surface). Therefore, marginalized likelihood for these parameters is nearly independent of the adopted model for the low redshift expansion history (i.e. whether Ω_{k}, or w are freely varied). Thus we are able to make use of the CMB information on the underlying linear matter power spectrum that is independent of the model for the low redshift expansion history, and does not contain information on the distance to the last scattering surface. By using the linear matter power spectrum as a 'standard ruler', we are able to infer information about the geometric parameters $D_V(z_{\mathrm{eff}})$ and F. In this case we run an MCMC chain with the following eight parameters, adding an additional multivariate Gaussian likelihood representing the CMB prior on the three linear matter power spectrum parameters: $\{\Omega_{\mathrm{c}} h^2, \Omega_{\mathrm{b}} h^2, n_{\mathrm{s}}, D_V(z_{\mathrm{eff}}), F, b\sigma_8, f\sigma_8, \sigma_{\mathrm{FoG}}^2\}$.

---

[6] A further subtlety is that to compute $\tilde{p}$, we restrict $\theta^\star$ to be sufficiently far from the hard prior boundary of σ_{FoG}^2, so that the volume element $\mathrm{d}\theta_{\mathrm{CMASS}}$ does not intersect the hard boundary. The difference between $\chi^2(\theta^\star)$ and the global χ^2 minimum is small, since σ_{FoG}^2 is poorly constrained by our measurements.

---

[5] http://lambda.gsfc.nasa.gov/product/map/dr4/parameters.cfm

This paper has been typeset from a TeX/LaTeX file prepared by the author.